# Short-pulse laser ablation of metals: Fundamentals and applications for micro-mechanical interlocking

Article

1 author:

Jeppe Byskov
Aarhus University
**12** PUBLICATIONS **463** CITATIONS

SEE PROFILE

# Short-pulse laser ablation of metals: Fundamentals and applications for micro-mechanical interlocking

JEPPE BYSKOV-NIELSEN

Department of Physics and Astronomy
University of Aarhus, Denmark

**PhD thesis**
August 2010

This thesis has been submitted to the Faculty of Science at Aarhus University in order to fulfill the requirements for obtaining a PhD degree in physics. The work has been carried out under the supervision of associate professor Peter Balling at the Department of Physics and Astronomy.

# Contents

# Acknowledgements

First of all I would like to thank Peter Balling for excellent supervision during my PhD. I have had the pleasure of being in contact with him on a very regular basis and he has always taken the time needed to discuss problems regarding my project. A big thanks to the members of the CATSUP group: Bjarke Christensen who trained me in the lab, when I joined the group in the beginning of 2006; Kristian Wædegaard with whom I did many of the experiments; Dang Le for LavVIEW assistance and other technical things. Also thanks to the rest of the group for fruitful discussions and for providing a good working atmosphere. Finally I would like to thank Folmer Lyckegaard for supplying me with all my samples and for assistance in the chemistry laboratory.

Turning to the Grundfos employees I owe great thanks to Jens Vestergaard Boll, Rune Højsholt and Allan Holm at Grundfos for participating in all parts of the project involving nanosecond laser structuring and micro mechanical interlocking. Also thanks to Marianne Greve Slot and Lis Eriksen at the material laboratory for their assistance with a number of different technical problems.

Last but not least I would like to thank Rasmus Byskov-Nielsen and Camilla Skinnerup for proofreading this thesis.

Jeppe Byskov-Nielsen

# List of publications

## Publications related to this thesis

- P. Balling, B.H. Christensen, J. Byskov-Nielsen and D.Q.S. Le
  *Laser-based Micro and Nanopackaging and Assembly II*
  eds. W. Pleging *et al.*
  SPIE, **6880**, DOI:10.1117/12.760049 (2008).

- J. Byskov-Nielsen and P. Balling
  *Laser structuring of metal surfaces: Micro-mechanical interlocking*
  Applied Surface Science, **255**, 5591 (2009)

- J. Byskov-Nielsen, J.V. Boll, A.H. Holm, R. Højsholt and P. Balling
  *Ultra-high strength micro-mechanical interlocking by injection molding into laser-structured surfaces*
  International Journal of Adhesion and Adhesives, **30**, 485 (2010)

- J. Byskov-Nielsen, J-M Savolainen, M.S. Christensen and P. Balling
  *Ultra-short pulse laser ablation of metals: threshold fluence, incubation coefficient and ablation rates*
  Applied Physics A, DOI 10.1007/s00339-010-5766-1 (2010)

- J. Byskov-Nielsen, J-M Savolainen, M.S. Christensen and P. Balling
  *Ultra-short pulse laser ablation of copper, silver and tungsten: experimental data and two-temperature model simulations*
  Applied Physics A, submitted (2010)

- J. Byskov-Nielsen, A.H. Holm, R. Højsholt, P. Sá and P. Balling
  *Testing the leak rate and corrosion resistance of micro-mechanically inter-locked joints*
  Journal of Colloid and Interface Science, submitted (2010)

## Additional publications

- H.B. Jeppesen, J. Byskov-Nielsen, P. Wright, J.G. Correia, L.M. Fraile, H.O.U. Fynbo, K. Johnston and K. Riisager
  *Alpha-decay half-life of 221Fr in different environments*
  The European Physical Journal A, **32**, 31 (2007)

- M.N. Christensen, J. Byskov-Nielsen, B.H. Christensen and P. Balling
  *Single-shot ablation of sapphire by ultrashort laser pulses*
  Applied Physics A, DOI 10.1007/s00339-010-5817-7 (2010)

- J. Byskov-Nielsen, B.H. Christensen, D.Q.S. Le, M.N. Christensen and P. Balling
  *Fundamentals of femtosecond laser ablation of dielectric materials*
  Proceedings of the 7th High-power Laser Ablation Conference
  (American Institute of Physics 2010)

# Outline of the thesis

**Chapter 1** gives a general introduction to pulsed laser ablation and highlights the differences between femtosecond and nanosecond ablation. Also a motivation of the work presented in this thesis is given.

**Chapter 2** presents an experimental investigation of femtosecond laser ablation of the metals copper, silver and tungsten. Incubation is discussed and related to the observed decrease in threshold fluence as more pulses are applied. Ablation rates and diameter measurements as a function of fluence are compared to theoretical estimates and the absorptance in both the high-fluence and the low-fluence regime is found.

**Chapter 3** compares the experimental findings of chapter 2 with simulations based on the two-temperature model (TTM). The dynamics of the laser-material interaction and the subsequent electron-phonon relaxation is modeled on a femtosecond timescale. Excellent agreement between data and simulation is observed when the TTM is extended to include ballistic electrons. The pulse duration dependence of the threshold fluence and melting depth is simulated and are found to be in agreement with approximate analytical expressions.

**Chapter 4** describes an experimental setup capable of measuring the ablation rate and reflectance of samples undergoing femtosecond laser structuring. This is done *in situ* and thus provides information about the ablation process during structuring. A model is proposed to explain the observed drop in reflectance and increase in ablation rate as multiple pulses are applied. The reflectance, scattering and absorptance as a function of the applied number of pulses are found by combining the model and the experimental data.

**Chapter 5** initiates the more applied part of the thesis. It describes experiments done on a nanosecond laser system with the aim to optimize the material removal rate. The detailed surface topography is shown to be highly dependent on both the laser parameters and the laser irradiation strategy. It is shown that the temperature dependence of the reflectance becomes important when nanosecond laser structuring is performed.

**Chapter 6** describes how laser surface structuring can be applied to generate new strong composite materials by employing micro-mechanical interlocking. The aim is to optimize the interlocking strength by varying the laser-generated surface geometry. We show that the interlocking between metal and plastic can be increased by several orders of magnitude by structuring as little as 10 mm$^2$. The joint strengths dependence on the depth of the holes and the distance between the holes is determined. Theoretical estimates of the strength are shown to be in good agreement with the experiments. Finally the fracture mechanism is determined.

**Chapter 7** continues the work presented in chapter 6, but focusses on the strength in the normal direction, i.e. the strength in the direction out of the holes, which is naturally much lower than the strength in the direction perpendicular to the holes. Again the joint strengths dependence on the depth of the holes and the distance between the holes is determined. The strength per structured area is shown to be about a factor of ten lower than in the perpendicular direction. Molten material is shown to be capable of closing up the holes, thereby providing a weak-point at which fracture can be initiated.

**Chapter 8** presents results from investigations regarding the corrosion resistance and water permeability of micro-mechanically interlocked samples. The permeability is shown to be consistent with the Hagen-Poiseuille equation independent of the laser structuring technique and is orders of magnitudes larger than the diffusion rate through the plastic. Corrosion tests show that care must be taken in order not to degrade the corrosion resistance of the sample to an unacceptable level.

**Chapter 9** gives a summary in English.

**Chapter 10** is a summary in Danish for people not familiar with the field of laser-material interaction.

# CHAPTER 1

## Introduction

In this chapter, a short introduction to pulsed laser ablation is given. Laser structuring of metal surfaces is a flexible and rapidly developing technology. Many of the material properties can be altered by tailoring the surface topography - for instance the optical, tribological, adhesive, chemical and biological characteristics can be controlled by intelligently designing the surface structures to match the need for a specific application. With short-pulse laser ablation the generated features can be controlled on the micrometer and even nanometer scale.

## 1.1   Introduction, motivation and contribution

The first working laser was demonstrated in 1960 [1] and during the past 50 years laser technology has developed into a billion dollar industry [2, 3]. In the beginning the laser was described as "a solution looking for a problem" but before long the unique qualities of the laser found numerous applications. Today lasers are everywhere, from laser-pointers and supermarket checkouts to space exploration and telecommunication.

The output of a laser can be continuous wave (CW) or pulsed. In pulsed operation, much higher peak powers can be achieved since the energy stored in the laser gain medium is released in a short burst. Laser ablation is the process of removing material from a surface by laser beam irradiation. Short pulse laser ablation is advantageous since the material can be heated up to the temperature of vaporization in a very short time. This means that the energy does not have time to spread into the deeper parts of the material and thereby the energy is localized where it is needed.

Vast resources have been invested in the development of new laser systems and specifications as for instance stability and power have increased immensely. For industrial applications stability is obviously a necessity but also the average power must be high since production time is of great concern. For laser surface structuring to be an industrially applicable technique, material removal rates of the order of 1 mm$^3$/s must be realized. As will be shown in chapter 5 this is achievable with commercial nanosecond lasers [4, 5].

Recent development has led to commercial picosecond lasers in the multi-10 W range [6] and on the research front a femtosecond multi-100 W laser has been demonstrated [7]. Ultra-short pulse lasers are thus maturing into systems applicable for industrial large area surface structuring. However, the interaction between metals and ultra-short laser pulses is still not fully understood. The research project presented in this thesis seeks to identify some of the fundamental questions of this interaction.

My contribution to the field of ultra-short pulse laser ablation is mainly to provide a better understanding of how specific metals respond when they are exposed to multi-pulse laser irradiation. When ablating with ultra-short laser pulses, only a very small amount of material is removed per pulse, so multi-shot ablation is in most cases a necessity. However, some material parameters change during the process, so a thorough investigation must be made to identify the exact ablation mechanisms. Experiments have been made on the metals copper, silver and tungsten and numerical simulations have been performed to compare theoretical models

with the data.

The main motivation for the work presented in the applied part of the thesis (chapter 5-8) is to optimize the efficiency of a specific component in a pump. This part is done in collaboration with the world's largest pump manufacturer, Grundfos A/S [8]. It is estimated that the efficiency of their submersible motors can be increased by 15% when replacing a metal component with a composite metal/polymer component. I have contributed to the process of achieving micro-mechanical interlocking (MMI) by laser surface structuring. By applying this technique we have demonstrated excellent adhesion between steel and plastic for use in the specific component. Since almost 20% of the world's electricity consumption is associated with pump systems [9], even small improvements of the efficiency can make a considerable impact.

## 1.2   Introduction to short-pulse laser ablation

The choice of laser system depends on the application at hand. First of all the structuring of metals, semiconductors and dielectrics is very diverse. Since ultra-short pulse lasers operate at very high intensities they can employ nonlinear absorption and are therefore an obvious choice for laser processing of transparent materials but it all depends on the specifications of the application [10, 11]. In this thesis only ablation of metals will be considered.

If structures on the tens of micrometers scale is the aim of the application, a nanosecond laser will often provide sufficient accuracy, and will typically have a greater throughput, thereby making it the preferred solution. If however, features on the nanometer scale is required, a pico- or femtosecond laser system would be a better choice.

For nanosecond laser systems the resolution of the generated features is limited by the heat diffusion length, $\ell \approx \sqrt{\kappa\tau}$, where $\kappa$ is the thermal diffusivity of the material and $\tau$ is the laser pulse duration [12]. Metals typically have a high thermal diffusivity and precise micro-structuring must therefore be undertaken with shorter pulses [13, 14]. It should also be noted that nanosecond laser processing is associated with a heat-affected zone, i.e. an area around the laser-generated hole where the temperature has been high enough for the material to undergo melting (but not vaporization). Though the material re-solidifies the strength of this area may have been greatly reduced.

For ultra-short pulse lasers the effect of heat propagation is very small. This implies that the energy is deposited over a length comparable to the optical penetration depth, $1/\alpha$, which is of the order of 10 nm for many metals. Very precise

structures can thus be made. However, a Gaussian laser beam cannot be focused by a lens to a smaller spot size than the diffraction limit [15]

$$\omega_0 = \frac{\lambda f}{\pi \omega_{lens}} \cdot \frac{1}{\sqrt{1 + f^2/z_0^2}} \approx \frac{\lambda f}{\pi \omega_{lens}}, \tag{1.1}$$

where $\omega_0$ is the minimum spot size, $f$ is the focal length of the lens, $z_0$ is the Rayleigh length and $\omega_{lens}$ is the spot size before the lens. Since $f/\omega_{lens}$ cannot practically be smaller than $\sim 1$, it is seen that the minimum feature size is of the order of the laser wavelength, $\lambda$. However, smaller features are possible due to the fact that materials undergoing femtosecond laser structuring exhibit a characteristic threshold for ablation called the threshold fluence. This means that a certain energy density must be exceeded before ablation is undertaken. Assuming a Gaussian intensity distribution of the laser focus, the diameter of the ablated structures can easily be shown to be

$$D^2 = 2\omega_0^2 \ln\left(\frac{F}{F_{th}}\right), \tag{1.2}$$

where $F$ is the fluence and $F_{th}$ is the threshold fluence. If the fluence is just slightly above the threshold it is seen that structures smaller than the minimum spot size can be generated. In this way structures down to a few hundred nanometers have been made [16, 17].

From the two-temperature model discussed in chapter 3 it can be shown that the ablation depth per laser pulse at low fluence can be expressed as

$$L = \ell \cdot \ln\left(\frac{F}{F_{th}}\right), \tag{1.3}$$

where $\ell$ is the effective penetration depth of the laser energy ($1/\alpha$ in the simplest approximation). This shows that when operating close to the threshold fluence only small amounts of material will be removed. Increasing the fluence yields a larger ablation depth but then heat propagation can also set in, even for femtosecond pulses.

To have a large material removal rate while preserving the nice features of the ultra-short pulse laser a low pulse energy in combination with a high repetition rate should be applied. This is exactly the observed tendency of newly developed cutting edge laser systems. For example, the 830 W femtosecond laser system reported by Eidam *et al.* [7] is operated at a repetition rate of 78 MHz. However, it has been demonstrated that particle shielding and heat accumulation effects must be considered at high repetition rates [18, 19].

Despite rapid development, much progress is still needed before ultra-short pulse laser systems can challenge nanosecond lasers for industrial large area surface structuring.

# Part I

# FEMTOSECOND LASER ABLATION OF METALS

# CHAPTER 2

---

# Ultra-short pulse laser ablation of copper, silver and tungsten

---

In this chapter femtosecond laser ablation studies of the metals copper, silver and tungsten are presented. Measurements of the threshold fluence determined from the hole diameters versus fluence provides incubation coefficients of the three materials, which are found to be equal within one standard deviation. Furthermore, we have determined the single-shot threshold fluences to be $1.7 \pm 0.3$ J/cm$^2$, $1.5 \pm 0.4$ J/cm$^2$, and $0.44 \pm 0.02$ J/cm$^2$ for copper, silver and tungsten respectively. These are in good agreement with theoretical values calculated neglecting heat diffusion.

The ablation rates in the regimes of high and low fluence have been examined. In the low-fluence regime, a logarithmic dependence has been found, while the high-fluence data are consistent with a linear dependence. A comparison of the high-fluence data with an approximate analytical solution provides the effective absorptance of the samples, i.e. the fraction of the laser energy that is contributing to the ablation process.

This chapter is based on the articles "Ultra-short pulse laser ablation of metals: threshold fluence, incubation coefficient and ablation rates", Applied Physics A, DOI 10.1007/s00339-010-5766-1 [20]

## 2.1   Introduction

The threshold fluence for ultra-short pulse laser ablation is an important parameter. For single-shot ablation, it is a parameter depending on the thermal and dynamical properties of the material. In the multi-shot scenario it is more complicated since incubation effects play a significant role.

Incubation can be seen in a number of different ways. For example it is observed that multi-shot ablation is possible for fluences below the single-shot threshold. The origin of the incubation is still under debate. One important factor is the energy coupling efficiency, which may be associated with the reduction in reflectance during the first laser pulses [21]. Laser induced surface plasmons and surface-scattered waves leading to the generation of ripples on the surface may be responsible for the increase in energy coupling. Chapter 4 will give a thorough description of the reflectance in relation to incubation, ripples, plasmons etc.

It is known that surface plasmons can only exist on a metal/air interface if the metal has a real part of the dielectric constant smaller than $-1$. Since tungsten has a positive value at 800 nm ($\epsilon_r^{W,800} = 5.22$) and thereby does not support surface plasmons while copper and silver do ($\epsilon_r^{Cu,800} = -24.1$, $\epsilon_r^{Ag,800} = -28.0$), it is interesting to compare the incubational behavior of these materials to examine whether surface plasmons play an important role.

This chapter also investigates the dependence of the ablation rate on the laser fluence, which is a topic of debate. Particularly at high fluence, where heat-propagation effects become significant, both a linear [22, 23] and a logarithmic [24, 25] dependence have been suggested.

## 2.2   Experiment

The laser applied for the experiments is a Ti:Sapphire based chirped pulse amplification (CPA) system delivering 100 fs pulses at a central wavelength of 800 nm. The beam is focused onto the sample using an $f = 45$ mm achromatic lens. In order to get an appropriate spot size, the sample is situated 500 $\mu$m behind the focus giving a 1/e spot size of approximately 40 $\mu$m. The repetition rate of the laser is varied between 10 Hz and 1 kHz and a mechanical shutter is applied to get the desired number of pulses (in the range from 1 to 1000). The material response to the radiation is independent of the repetition rate since 1 ms is much longer than the other time scales considered in the ablation process. At low repetition rate the pulse energy is measured with a calibrated photodiode whereas a powermeter is used at higher repetition rates. The applied pulse energies are in the range from 9

to 185 $\mu$J.

The samples are mechanically polished to a very low surface roughness. Hereby the initial reflectance can be approximated with the Fresnel reflectance $R_f = |\frac{\tilde{n}-1}{\tilde{n}+1}|$, where $\tilde{n}$ is the complex refractive index. The real and imaginary parts can be found in Ref. [26] and interpolation is applied to find these at the desired wavelength. We find reflectances at 800 nm to be 0.960, 0.981 and 0.496 for copper, silver and tungsten respectively.

The diameter of the ablated structures are found using a scanning electron microscope (SEM), while the depth has been found using optical microscopy (focusing respectively on the edge and the bottom of the hole).

## 2.3 Results and discussion

We want to examine the material response to femtosecond laser irradiation in two different ways. The first is based on measurements of the diameter of the ablated holes, while the second one is based on measurements of the depth.

### 2.3.1 Diameter measurements

Figure 2.1 shows a plot of the diameter squared versus the applied pulse energy. The number of applied pulses is in the range from 1 to 1000 and some have been omitted from Fig. 2.1 for clarity.

The solid lines represent least square fits to the equation

$$D_i^2(N) = 2\omega_i^2 \ln\left(\frac{E_{pulse}}{E_{th}(N)}\right). \tag{2.1}$$

This expression is valid if we assume that the laser beam has a Gaussian intensity distribution, heat propagation effects can be neglected and ablation occurs only when a certain threshold energy is exceeded [27].

Since the laser beam is slightly elliptical, as can be seen in Fig. 2.2, the equation is divided in two parts representing the major and minor axis ($i = maj, min$). $D_i$ is thus the major/minor axis of the holes, $\omega_i$ the major/minor axis of the laser spot size and $E_{th}$ the threshold pulse energy which must be exceeded for material removal to set in. Note that $E_{th}$ must be the same for the two axes.

The threshold pulse energy is found for a series of different number of applied pulses. In order to find the threshold fluence we apply

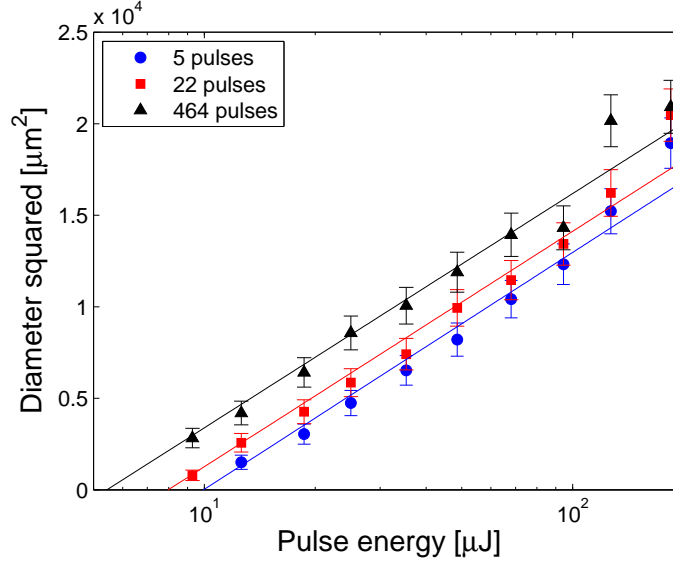$$F_{th}(N) = \frac{2E_{th}(N)}{\pi\omega_{maj}\omega_{min}}. \tag{2.2}$$

**Figure 2.1.** *Hole diameters squared versus the laser pulse energy for different numbers of applied pulses on a tungsten sample. The plots for 1, 10, 46, 100, 215 and 1000 pulses have been omitted for clarity. Solid lines represent fits to Eq. (2.1).*

We are now able to plot the threshold fluence versus the number of applied pulses, see Fig. 2.3.

The solid line represents a least square fit to the equation

$$F_{th}(N) = F_{th}(1) \cdot N^{S-1}, \tag{2.3}$$

as proposed by Jee *et al.* [28]. $S$ is the so-called incubation coefficient, which quantifies the degree of incubational behavior. $S = 1$ corresponds to no incubation effect and $S < 1$, which is usually observed, corresponds to a decrease in threshold fluence as more pulses are applied. It is clear that this equation is only valid for a limited number of pulses, since the threshold fluence cannot keep on decreasing. It is therefore reasonable to exclude points from the fit where the threshold fluence has reached its final value. The results are summarized in table 2.1.

A simple theoretical value for the single-shot threshold fluence is found by assuming that the light is absorbed according to Beers law (exponentially with a characteristic absorption length $1/\alpha$) and that ablation occurs when the energy per unit volume exceeds the energy necessary for the material to undergo heating, melting and evaporation. This energy can often be well approximated by its dominating term, the enthalpy of evaporation per unit volume $\Delta H_{vap}$. Taking into considera-
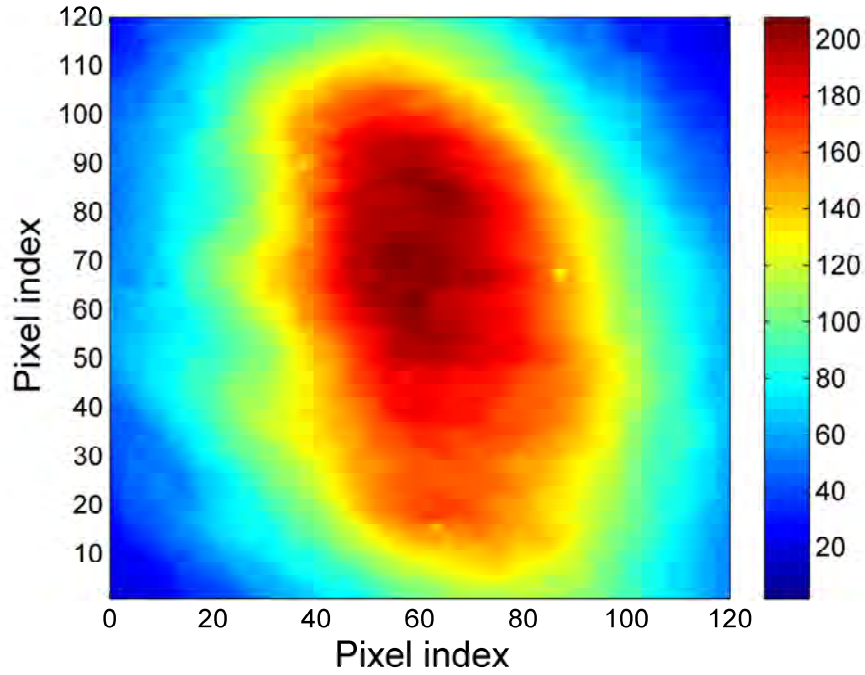
**Figure 2.2.** *Measurement of the laser beam profile recorded on a CCD detector. The beam is seen to be slightly elliptical and $\omega_i$ is therefore introduced as described in the text.*

**Table 2.1.** *Enthalpy of evaporation, optical penetration depth, absorptance, theoretical threshold fluence, measured threshold fluence and measured incubation coefficient of the three materials. The theoretical threshold fluence is calculated from Eq. (2.4)*

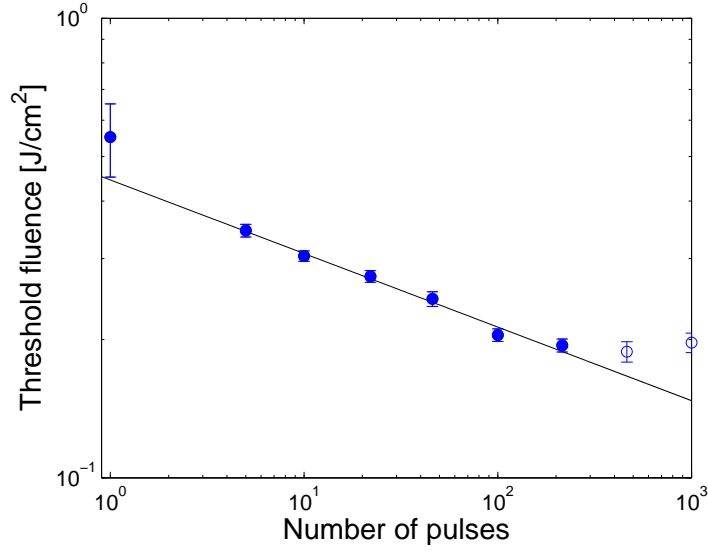|  | Cu | Ag | W |
|---|---|---|---|
| $\Delta H_{vap}$ [GJ/m$^3$] | 42.2 | 24.4 | 86.5 |
| $1/\alpha$ [nm] | 13 | 12 | 23 |
| $A_{initial}$ | 0.040 | 0.019 | 0.50 |
| $F_{th}^{theo}(1)$ [J/cm$^2$] | 1.38 | 1.51 | 0.40 |
| $F_{th}^{data}(1)$ [J/cm$^2$] | $1.7 \pm 0.3$ | $1.5 \pm 0.4$ | $0.44 \pm 0.02$ |
| $S^{data}$ | $0.85 \pm 0.03$ | $0.87 \pm 0.05$ | $0.84 \pm 0.01$ |

**Figure 2.3.** *Threshold fluence versus the number of applied pulses on a tungsten sample. Only the filled data points are used in the fit to Eq. (2.3).*

tion that only a fraction $A$ of the light is actually absorbed, the threshold fluence can be expressed as

$$F_{th} = \frac{\Delta H_{vap}}{\alpha A},$$ (2.4)

As will be the topic of chapter 4, an often neglected problem is the fact that the absorptance of the sample changes dramatically during multi-pulse ablation. The single-shot ablation threshold fluence can however be found by applying $A_{initial} = (1 - R_{initial})$ with the initial reflectance equal to the Fresnel reflectance. Inserting tabulated numbers one finds the values listed in table 2.1. It is seen that we have good agreement between experiment and theory, although the threshold fluence of copper has previously been reported to be somewhat lower [24, 29] than the present value. It must be remembered, however, that it is the absorbed fluence that affects the material. In Ref. [29] the absorbed threshold fluence is reported to be $(59\pm10)$ mJ/cm$^2$ in excellent agreement with our value of $F_{abs} = F \cdot A = (1.7\pm0.3)$ J/cm$^2 \cdot$ 0.04 $= (68\pm12)$ mJ/cm$^2$. In Ref. [24] a value of the absorbed fluence is not provided nor is a value of the absorptance, but assuming that their sample has an initial absorptance of 10%, agreement with our data is obtained.

A theoretical expression for the incubation coefficient is not existent, nor is a description of which materials should exhibit a larger incubational behavior. One
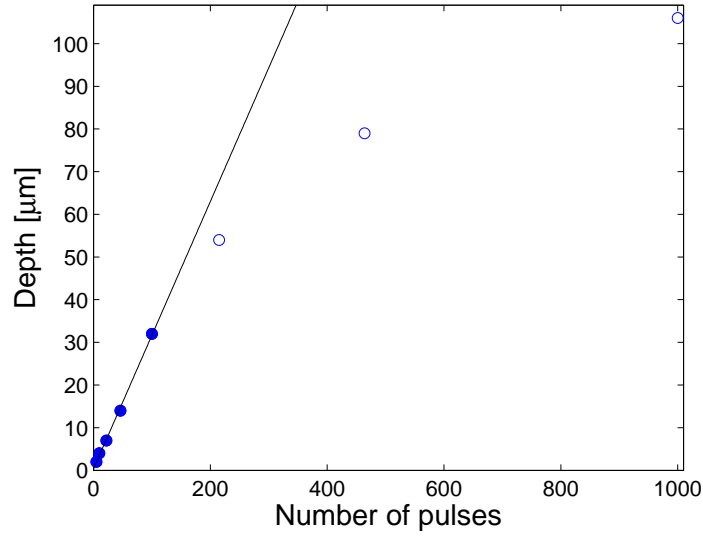
**Figure 2.4.** *The depth of the holes versus the number of applied pulses on a copper sample. Filled data points are used to find the ablation rate.*

might expect that materials with a high Fresnel reflectance would have a rapidly decreasing threshold fluence since the reflectance drops drastically during the first few pulses. Also one could expect that the excitation of surface plasmons would play a role, since they may provide an extra energy incoupling mechanism.

Nevertheless the data show that the measured incubation coefficients are equal within one standard deviation, so no significant difference is evident. This indicates that Fresnel reflectance and surface plasmons do not have a major effect on the incubational behavior of the material. However we cannot rule out the possibility that the two effects cancel each other out. The incubation coefficient of copper found in the present investigation is in excellent agreement with the value $0.87 \pm 0.02$ from Ref. [24] but deviates from the $0.76 \pm 0.02$ of Ref. [29].

### 2.3.2 Depth measurements

Measurements of the depth of the ablated holes can also provide important information about the material response to femtosecond laser irradiation. When plotting the depth of the holes as a function of the number of applied pulses, the average amount of material removed per pulse can be found from the slope, see Fig. 2.4.

It is seen that the rate decreases when more than ∼100 pulses are applied. This happens when hole depths become comparable to the laser spot size, since
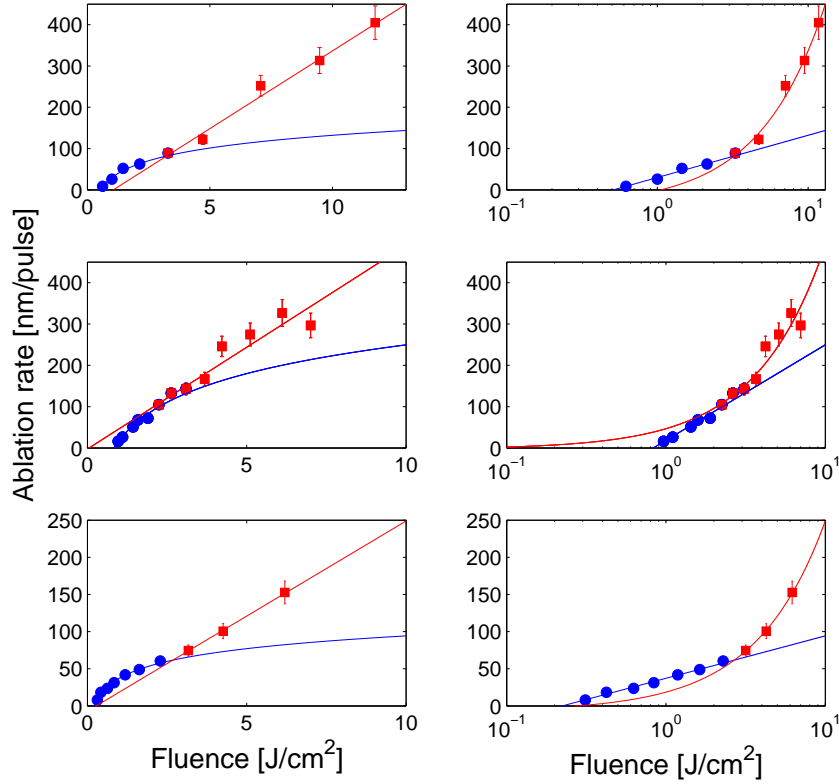
**Figure 2.5.** *Ablation rate versus fluence on a linear scale (left) and logarithmic scale (right). The materials from top to bottom are copper, silver and tungsten. The blue line represent least square fits to Eq. (2.5) and the red line a fit to Eq. (2.6).*

the laser energy is then distributed over a larger area, leading to a smaller effective fluence. At even greater depths, other effects come into play [30]. The ablation rate is determined from a fit to the linear region. This is done for approximately 10 different pulse energies.

Figure 2.5 shows plots of the ablation rate as a function of the applied fluence. In the left column the plots are on a linear fluence scale and in the right on a logarithmic scale. Two different regimes at low and high fluence are clearly identified.

**Table 2.2.** *Effective penetration depth, threshold fluence and absorptance of the three materials.*

|                      | Cu            | Ag            | W             |
| -------------------- | ------------- | ------------- | ------------- |
| $\ell$ [nm]          | $44 \pm 4$    | $100 \pm 6$   | $25 \pm 1$    |
| $F_{th}$ [J/cm$^2$]  | $0.51 \pm 0.02$ | $0.83 \pm 0.02$ | $0.22 \pm 0.01$ |
| $A_{low}$            | 0.368         | 0.294         | 0.960         |

#### 2.3.2.1   Low-fluence regime

In the low-fluence regime (blue circles in Fig. 2.5) the data appear to follow a logarithmic dependence on the applied laser fluence. Consequently, the data are fitted to the expression

$$L_{low} = \ell \cdot \ln \left( \frac{F}{F_{th}} \right) \tag{2.5}$$

where $\ell$ is the effective penetration depth of the laser energy. The penetration depths and threshold fluences found from the fits are summarized in table 2.2. Note that the threshold fluence is not the single-shot threshold fluence, since it represents an average ablation rate during the first 100 pulses. The values are in fair agreement with the values determined in Sec. 2.3.1 after $\sim$100 pulses.

The effective penetration depths for the noble metals are seen to be much larger than the optical penetration depths of 13 nm and 12 nm for copper and silver respectively, while for tungsten the value is in good agreement with the theoretical 23 nm [26]. We attribute the difference mainly to ballistic electrons [31], although it has also been pointed out previously that the greater absorption depths may in part be due to the fact that heat propagation cannot be fully neglected [23]. The role of ballistic electrons will be discussed in chapter 3.

By comparing the measured threshold fluence with Eq. (2.4), where $1/\alpha$ is replaced by the effective penetration depth $\ell$, the data can provide a measure for the effective absorptance of the metals during the first $\sim$100 pulses. These are given in table 2.2. For all three metals these values clearly exceed one minus the Fresnel reflectance and thus support the suggestion that increasing absorptance is an important factor for incubation effects. Note that the absorptance of tungsten is approaching 100%, which is consistent with a recent observation [32].

#### 2.3.2.2  High-fluence regime

In the high-fluence regime (red squares in Fig. 2.5) heat propagation becomes significant. This regime has previously been investigated [22, 23]: Computer simulations of the two-temperature model [33] predicted a linear dependence at high fluence. In addition, the observation from the simulations that thermal equilibrium between electrons and lattice takes place after some picoseconds, led to an analytical model, which is approximately valid when most of the heat transport occurs with electron- and lattice temperatures in equilibrium [22, 23]. This will be discussed in more detail in the next chapter when the two-temperature model simulations are presented.

The energy is assumed to be deposited as a delta function in time and in a thin sheet at the surface. This is a good approximation for a laser spot size larger than the optical penetration depth and the heat diffusion length, which is the case in the present setup. Applying the ablation criterion $CT \geq \Delta H_{vap}$, where $C$ and $T$ are the heat capacity and temperature of the equilibrated system respectively, an expression for the ablation rate in the high-fluence regime is obtained [22, 23]:

$$L_{high} = \sqrt{\frac{2}{\pi e}} \frac{A_h F}{\Delta H_{vap}}. \qquad (2.6)$$

The claim that the ablation rate grows *linearly* with fluence and not logarithmic is at variance with other reports [24, 25]. As can be seen from Fig. 2.5, the present data are in excellent agreement with a linear ablation rate at high fluence for all three materials, although a logarithmic growth cannot be completely excluded.

By comparing the slope of the curve with Eq. (2.6), the effective absorptance at high fluence is found to be 0.329, 0.248 and 0.457 for copper, silver and tungsten respectively. For copper and silver the absorptance in the high-fluence regime is comparable to the absorptance in the low-fluence regime, which can be taken to support the validity of the linear model. For tungsten the absorptance is, however, significantly lower than for the low-fluence data. This may be due to limitations in the linear model, or it may reflect the phenomenon that the remarkably high absorptance in the low-fluence regime is a consequence of a very specific surface topography [32], which cannot be maintained in the high-fluence regime where a significant surface melting is expected [21].

## 2.4  Conclusion

We have studied femtosecond laser ablation of the metals copper, silver and tungsten.

From measurements of the ablated hole diameters, we have found single-shot threshold fluences in good agreement with theoretical estimates. The incubation coefficients of the three materials are equal within one standard deviation, implying that surface plasmons and the initial Fresnel reflectance do not play a major role in determining the incubational behavior of the material.

From measurements of the ablated hole depths, we find the fluence dependence of the ablation rate to be logarithmic at low fluence while it changes to a linear dependence at higher fluence. The two regimes are compared to analytical expressions derived from approximations to the two temperature model, which provides the absorptance of the samples in both the high- and low-fluence regime.

# CHAPTER 3

# Comparing two-temperature model simulations with experimental data

In chapter 2 experimental femtosecond laser ablation studies of the metals copper, silver and tungsten were presented. In this chapter the experimental findings are compared with simulations based on the two-temperature model. The data are shown to be in good agreement with the simulations. The comparison provides new information about the laser-heating process: For the noble metals (Cu, Ag) energy transport via ballistic electrons must be included while this effect is negligible for a transition metal (W). The comparison provides values for the range of ballistic electrons in the noble metals. The model calculation is also employed to investigate the dependence of the threshold fluence and melting depth on pulse duration. It is observed that for pulses shorter than approximately 1 ps the threshold fluence and melting depth are independent on the pulse duration, while they increase as $\tau^{0.47}$ and $\tau^{0.51}$, respectively, for pulses longer than $\sim 40$ ps, in good agreement with approximate analytical expressions predicting a $\sqrt{\tau}$ dependence.

This chapter is based on the article "Ultra-short pulse laser ablation of copper, silver and tungsten: experimental data and two-temperature model simulations", submitted to Applied Surface Science.

## 3.1   The Two-Temperature Model

The two-temperature model (TTM) attempts to describe the dynamics of metals after short-pulse laser irradiation [33]. By solving two coupled differential equations for the electron and lattice temperatures the ultra-fast dynamics of the interaction is modeled. The two equations can be written

$$C_e \frac{\partial T_e}{\partial t} = \nabla \cdot \{\kappa_e \nabla T_e\} - \Gamma\{T_e - T_l\} + Q \qquad (3.1)$$

$$C_l \frac{\partial T_l}{\partial t} = \nabla \cdot \{\kappa_l \nabla T_l\} + \Gamma\{T_e - T_l\}, \qquad (3.2)$$

where $C_e$ and $C_l$ are the heat capacities and $\kappa_e$ and $\kappa_l$ the heat conductivities of the electron and lattice systems, respectively. $\Gamma$ is the electron-phonon coupling strength, and $Q$ is the laser source term given by the expression

$$Q = \alpha A I(t) e^{-2r^2/\omega^2} e^{-\alpha z}. \qquad (3.3)$$

Here $1/\alpha$ can be identified as the optical penetration depth, $A$ is the absorptance of the sample and $\omega$ is the laser spot size. $I(t)$ is, in the present investigation, given by a Gaussian distribution.

Since $\kappa_l \ll \kappa_e$, heat diffusion in the lattice system is safely neglected and the ions therefore only exchange energy locally with the electrons. If the laser spot size is much larger than the depth of the ablated structures, the three-dimensional equations reduce to two coupled one dimensional equations, since it can be assumed that all the energy is propagating into the material and not along the surface.

The electron-phonon coupling, $\Gamma$, has often been considered to be constant or linearly increasing with temperature, see e.g. Refs. [22] and [23]. However, more detailed calculations based on the electronic density of states show that $\Gamma$ has a complicated dependence on temperature [34]. In the present calculations we have therefore used the electron-phonon coupling strengths computed in Ref. [34]. The electron-phonon coupling is, however, only computed up to 50.000 K, so above this temperature an extrapolation has to be applied. While there is *a priori* no simple extrapolation function, in the present investigation a $T^{-2/3}$ dependence will be assumed, as this expression provides a smooth extrapolation of the calculated values (see Fig. 3.1) and incorporates the physical expectation of a vanishing coupling strength at very high temperatures.

Different extrapolations were tested and it was found to only marginally influence the results of the computation. Generally the results of the simulations become more uncertain at high temperature, since the validity of the TTM model
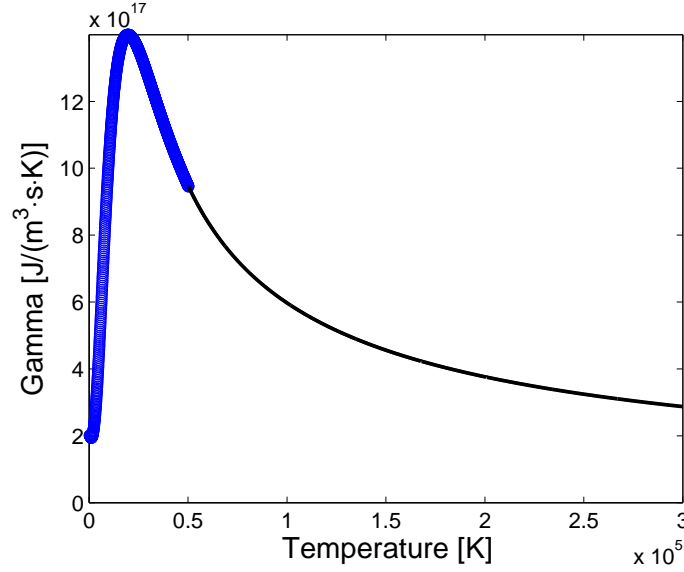
**Figure 3.1.** *The electron-phonon coupling strength versus temperature for tungsten. The blue squares represent the values computed in Ref. [34] while the black solid line represents the $T^{-2/3}$ extrapolation function.*

is questionable at very high fluence (i.e. high temperature). The limited validity of the TTM has been discussed in numerous references, see e.g. [35], [36] and [37].

## 3.2   Results and discussion

The TTM equations are solved numerically in MATLAB. Initial electron and lattice temperatures are 300 K throughout the sample and the time steps are adjusted dynamically to achieve the specified accuracy.

In the spatial coordinate 1000 points are logarithmically distributed from the surface and down to a depth of 2 $\mu$m. This ensures good resolution near the surface where the spatial variation in temperature is largest.

Solving the TTM equations yields the electron and lattice temperatures as a function of time and depth in the sample. A typical result of such a calculation, for a pulse duration of 100 fs, is shown in Fig. 3.2.

In Fig. 3.2(a) it can be seen how the electron system is heated on the femtosecond time scale and that a maximum electron temperature of more than 40.000 K is reached on the surface after approximately 100 fs. For fluences close to the threshold fluence, the optical penetration depth (13 nm in the case of copper) de-
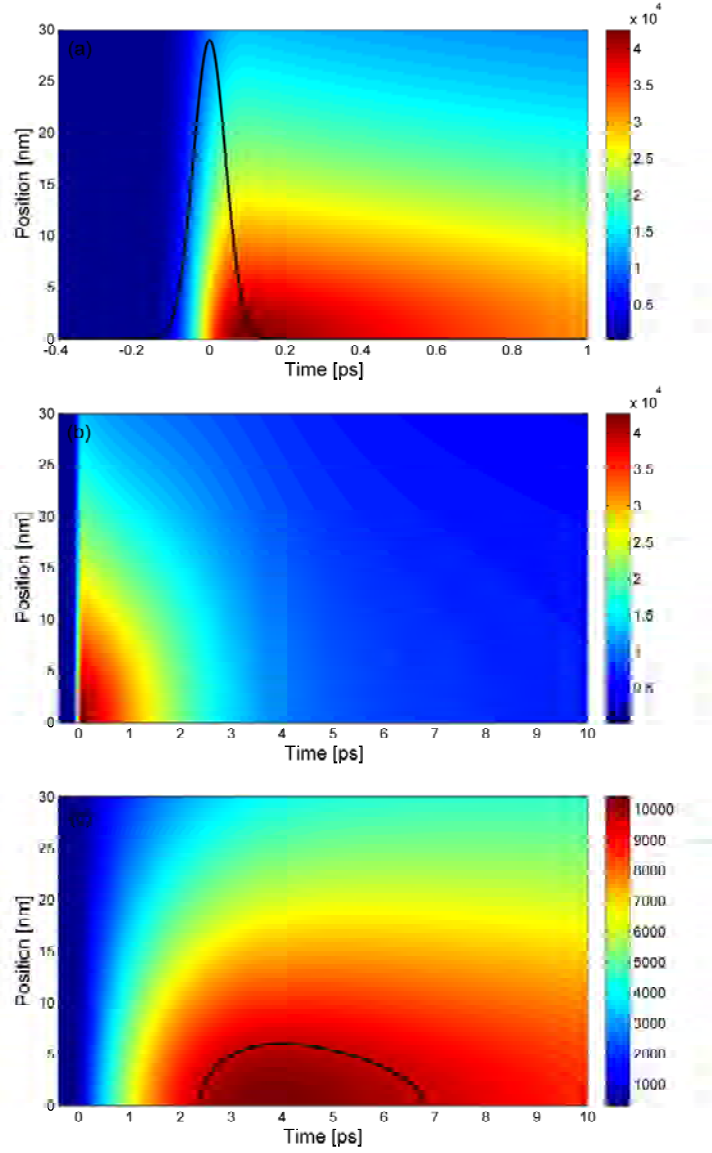
**Figure 3.2.** *Electron [(a) and (b)] and lattice (c) temperature versus time and position into a copper sample for an absorbed fluence just above the threshold for ablation (0.14 J/cm$^2$). Panel (a) shows a close-up of the first picosecond, where the black line represents the intensity envelope of a 100 fs Gaussian laser pulse centered at 0 ps. As can be seen from (b) and (c), the energy is transferred from the electrons to the lattice on a timescale of some picoseconds. The black line in the bottom plot indicates the ablation temperature according to Eq. (3.4). In the case of copper the ablation temperature is 10425 K.*
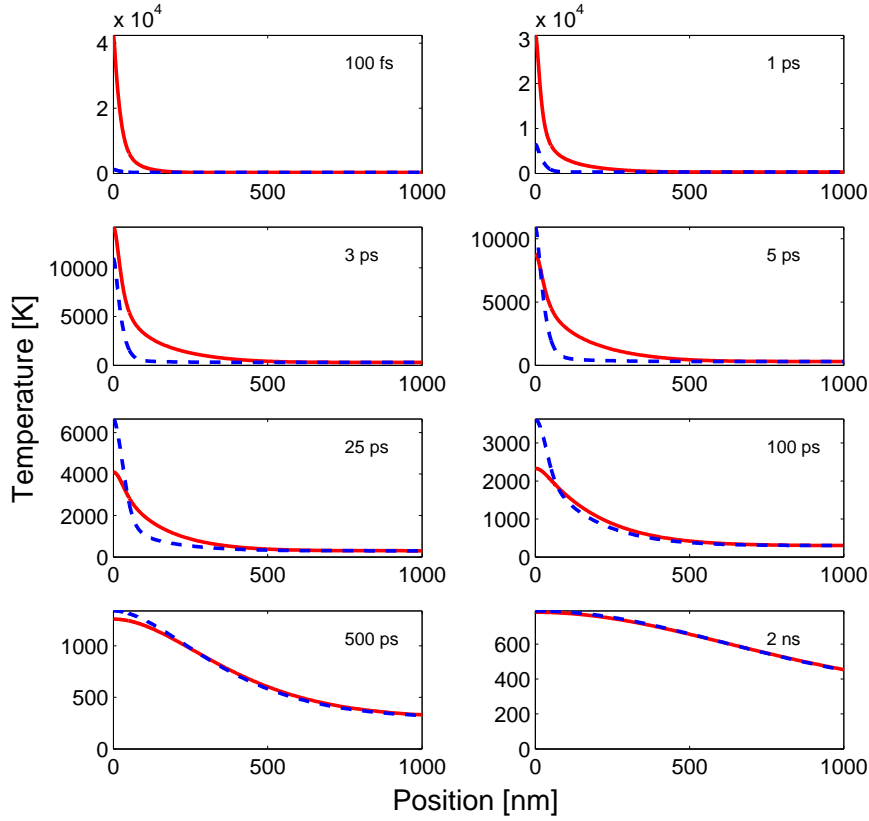
**Figure 3.3.** *Electron (red solid line) and lattice (blue dashed line) temperature versus the position into a copper sample at various times. The absorbed fluence is 0.14 J/cm² and the applied pulse length is 100 fs.*

termines the range over which the energy is distributed. Figure 3.2(c) illustrates how the lattice remains cold for the first few picoseconds and is then heated via electron-phonon collisions over a timescale of a few picoseconds. The plots shown in Fig. 3.3 represent vertical cuts (i.e. different times) of the electron (red) and lattice (blue) temperature.

It is seen that thermal equilibrium between electrons and lattice is established after a few picoseconds. Heat diffusion in the electron system transfers energy to the deeper parts of the sample resulting in the electron temperature being lower than the lattice temperature at subsequent times.

At higher fluences an approximate electron-lattice equilibrium is observed after a few tens of picoseconds, and the energy is distributed over hundreds of nanome-

ters due to heat propagation effects, see Fig. 3.4. Notice the much higher temperatures reached at this fluence compared to the low-fluence scenario displayed in Fig. 3.2. As discussed in the introduction, one of the desired features of the femtosecond laser is the very localized energy deposition. The results of the simulations shown in Fig. 3.4 demonstrate that this feature must be given up when operating at fluences much higher than the threshold fluence.

The ablation temperature, indicated by the black lines in Figs. 3.2(c) and 3.4(b), is determined from the ablation criterion. We assume that ablation takes place when the combined energy of the electron and lattice systems exceeds the energy needed for the material to undergo heating, melting and evaporation. Numerically we neglect the contribution from heating and melting, since the energy required for evaporation ($\Delta H_v$) is much larger than these. As heat propagation in the lattice system is neglected, the lattice can only receive energy locally from the electrons. The maximum energy density at a certain point is therefore attained when the maximum lattice temperature is reached, i.e. when the electron and lattice systems are in equilibrium. The ablation criterion can thus be written as

$$C_l T_{l,max} + \frac{C_e'}{2} T_{l,max}^2 \geq \Delta H_v, \qquad (3.4)$$

where the heat capacity of the electrons is considered to be linear in temperature, i.e. $C_e = C_e' T_e$.

Note that in the two-temperature model calculation, the heat is allowed to propagate further even after the lattice obtains the ablation temperature at the maximum depth. However, the ablation depth is in the present description taken to be this maximum depth. This is chosen because the model lacks a description of the dynamics of the ablation process, which will of course strongly influence the response of the material at these high excitation levels and longer propagation times. Inspired by a molecular-dynamics description of ablation [38], one could say that the present ablation criterion corresponds to the assumption that spallation will take place at the maximum depth where the heat content exceeds the enthalpy of evaporation.

For a pulse duration of 100 fs, as applied in Figs. 3.2 and 3.4, the highest electron temperature is reached after approximately the pulse duration. At this time the lattice is still cold (300 K). The electron temperature rapidly decreases as energy is transferred partly via electron-phonon collisions to the lattice and partly via heat conduction to the deeper parts of the sample. The simulations are propagated for sufficiently long time that the ablation criterion is no longer fulfilled anywhere in the sample.
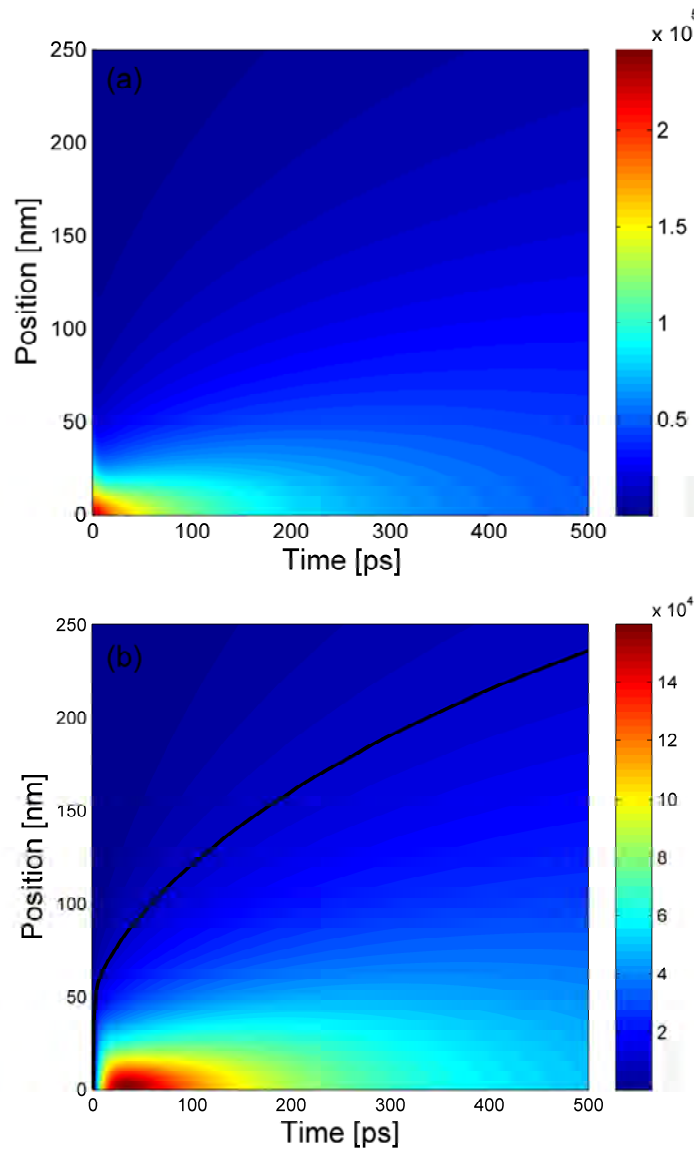
**Figure 3.4.** *Electron (a) and lattice (b) temperature versus time and position into a copper sample for an absorbed fluence of 4.06 J/cm$^2$. The black line indicates the ablation temperature according to Eq. (3.4)*

By changing the absorbed fluence used in the simulations, the ablation depth at different fluences can be found. This is shown by the black curves in Fig. 3.5 for the metals copper, silver and tungsten.

The blue and red curves in Fig. 3.5 correspond to analytical low-fluence and high-fluence approximations, respectively. To obtain an analytical expression in the low-fluence regime one often neglects heat diffusion in both the lattice system and in the electron system. An expression for the ablation depth is then easily found to be

$$L_{low} = \frac{1}{\alpha} \ln \frac{F}{F_{th}},$$
(3.5)

where the threshold fluence is given by $F_{th} = \Delta H_v / A\alpha$.

In the high-fluence limit an analytical approximation can be obtained by assuming that most of the heat transport occurs in thermal equilibrium between electrons and lattice. Equations 3.1 and 3.2 then reduce to one equation governing the equilibrated system where the heat capacity of the system is approximated with the heat capacity of the lattice. Solving this equation yields an analytical expression for the high-fluence ablation rate

$$L_{high} = \sqrt{\frac{2}{\pi e}} \frac{AF}{\Delta H_v}.$$
(3.6)

A more detailed derivation and discussion of equations (3.5) and (3.6) are given in references [22] and [23].

The low-fluence approximation clearly underestimates the ablation depth at higher fluences since it does not account for heat propagation into the deeper parts of the sample. For the noble metals it is also seen to somewhat underestimate the threshold fluence found from the simulated data. This is partly due to ballistic electrons as will be discussed later.

The high fluence approximation can be seen to overestimate the ablation depth slightly, since it neglects the electronic contribution to the heat capacities. As the electron heat capacity grows linearly with temperature this becomes increasingly important at higher fluences, in good agreement with the results shown in Fig. 3.5.

### 3.2.1   Pulse-duration dependence of the threshold fluence

Experiments have shown that the threshold fluence depends on the laser pulse duration [39, 40]. Figure 3.6(a) shows the result of a series of simulations for copper, where the pulse duration has been varied through the term $I(t)$ in Eq. (3.3) and
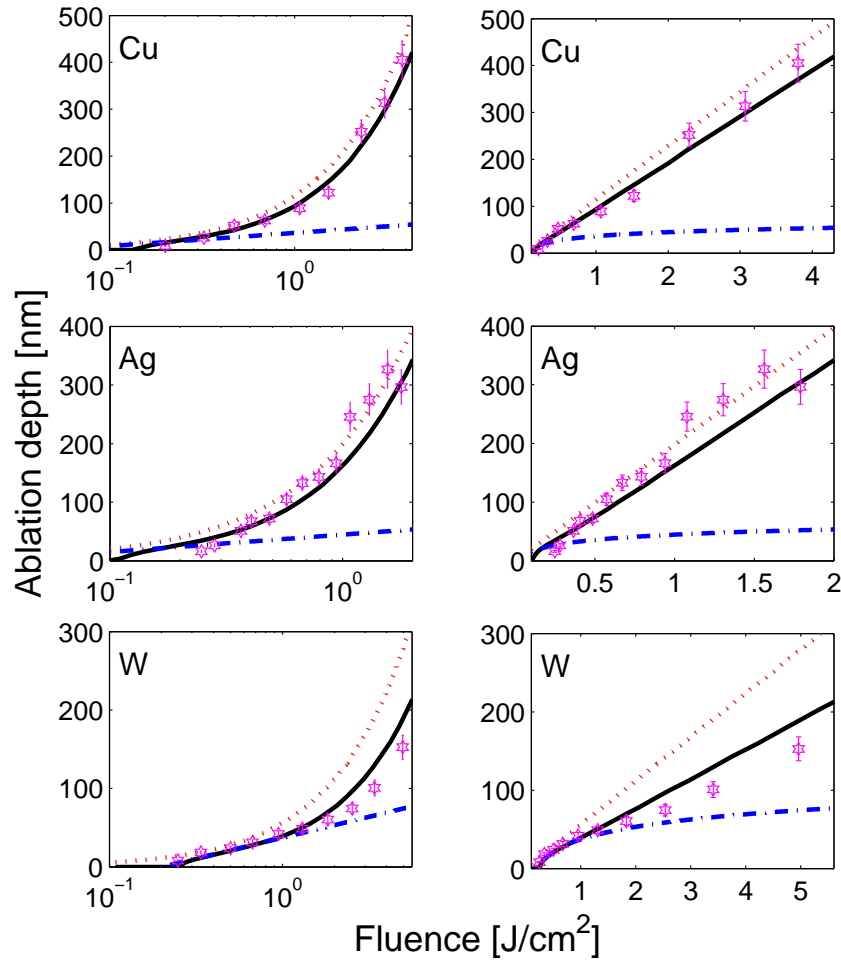
**Figure 3.5.** *Depth of the ablated holes versus the absorbed fluence for copper, silver and tungsten samples. The purple stars are the experimental data points, the blue dash-dotted line the low fluence analytical expression from Eq. (3.5), the red dotted line the high fluence analytical expression from Eq. (3.6) and the black solid line the results of the TTM simulations.*

the threshold fluence has been found, by carrying out calculations similar to those shown by the black line in Fig. 3.5, for each value of the pulse duration.

It can be observed that the threshold fluence is independent on the pulse duration for pulses shorter than 1 ps (red dashed line in Fig. 3.6(a)). This is consistent with previous theoretical and experimental investigations on gold [41] and reflects the observation that when the pulse duration is shorter than the characteristic electron-lattice coupling time, the exact duration becomes unimportant. On the other hand, for longer pulses, the threshold fluence increases and becomes proportional to $\tau^{0.47}$ for pulses longer than $\sim 40$ ps (green dash-dotted line in Fig. 3.6(a)).

From Eqs. (3.1) and (3.2), fundamental timescales of the interaction can be estimated. The lattice heating time is $\tau_l = C_l/\Gamma \approx 35$ ps, if a typical value of $10^{17}$ Jm$^{-3}$s$^{-1}$K$^{-1}$ is chosen for the electron-phonon coupling strength. Similarly, a diffusion time, i.e. the time needed for heat diffusion to become comparable to the optical penetration depth, is estimated as $\tau_d = (1/\alpha)^2 C_l/\kappa = 1.5$ ps, see also Ref. [39]. These values are seen to be in good agreement with the different regimes observed in the present experiment, i.e. a constant value of the threshold fluence for pulse durations below $\tau_d$ and a $\sqrt{\tau}$ dependence for pulse durations longer than $\tau_l$.

The observed value of the threshold fluence for pulses shorter than 1 ps is 127 mJ/cm$^2$. This is about a factor of 2 larger than the approximate analytical expression $F_{th} = \frac{\Delta H_{vap}}{\alpha A}$ discussed in section 2.3.1. Heat diffusion in the electron system, which is neglected in the derivation of the analytical expression, is responsible for the difference. This indicates that heat propagation cannot be neglected even at the threshold fluence.

Applying the same approximations that led to Eq. (3.6), it can be assumed that the temperature distribution for an ultra-short pulse is a delta function in both time and space [23]

$$T_\delta(z, t) = \frac{2F}{C} \sqrt{\frac{C}{4\pi\kappa t}} \exp\left(-\frac{Cz^2}{4\kappa t}\right). \tag{3.7}$$

If we assume that the heat-propagation equations are linear (which is only approximately true) a Gaussian pulse can then be described as an integral over contributions like Eq. (3.7):

$$T_{Gauss}(z, t) = \int_{-\infty}^{t} I(t') \frac{T_\delta(z, t - t')}{F} dt'. \tag{3.8}$$

Inserting $I(t')$ and $T_\delta(z, t - t')$ into this expression and taking the value at the surface ($z = 0$) yields
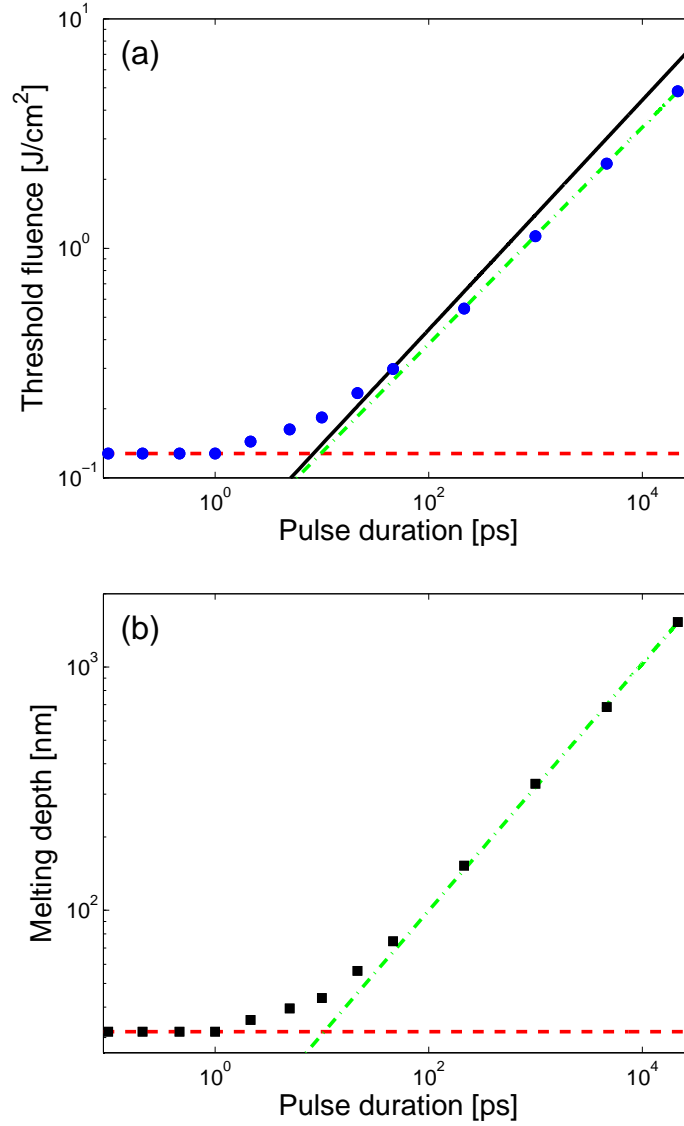
**Figure 3.6.** *(a) The calculated threshold fluence for copper versus the laser pulse duration (blue circles). (b) The calculated melting depth for copper at the threshold fluence versus the laser pulse duration (black squares). Three regimes are seen: A constant value below 1 ps, a transition region and then a power law at longer pulse durations. The red dashed line is a fit to the data points below 1 ps and the green dash-dotted line a fit to the data $\geq$ 40ps. The black solid line in (a) represents an analytical expression given by Eq. (3.11).*

$$T_s(t) = \frac{2I_0}{\sqrt{4\pi\kappa C}} \int_{-\infty}^{t} \exp\left(-4\ln 2 \left(\frac{t'}{\tau}\right)^2\right) \frac{1}{\sqrt{t-t'}} dt'. \qquad (3.9)$$

Applying the substitutions $\Theta = \sqrt{4\ln 2}\frac{t}{\tau}$ and $\Theta' = \sqrt{4\ln 2}\frac{t'}{\tau}$ produces a dimensionless integral, which can be solved numerically to provide the surface temperature as a function of time:

$$T_s(\Theta) = \frac{2I_0}{\sqrt{4\pi\kappa C}} \sqrt{\frac{\tau}{\sqrt{4\ln 2}}} \int_{-\infty}^{\Theta} \exp\left(-\Theta'\right)^2 \frac{1}{\sqrt{\Theta-\Theta'}} d\Theta'. \qquad (3.10)$$

The maximum surface temperature can now be found, and this expression can readily be inverted to provide the threshold fluence as a function of the pulse duration:

$$F_{th,long} = \frac{\pi C T_{abl}}{2.1524\sqrt{\sqrt{4\ln 2}}} \sqrt{\frac{\kappa\tau}{C}}. \qquad (3.11)$$

Here $C$ is approximated with the lattice contribution to the heat capacity and $\kappa$ is approximated with $\kappa_0$. The factor 2.1524 arises from the maximum of the dimensionless integral in Eq. (3.10).

As expected, the analytical expression gives a $\sqrt{\tau}$ dependence. It can be seen from the black solid line in Fig. 3.6(a) that there is a reasonable agreement between Eq. (3.11) and the simulated data at longer pulse durations, though it seems to slightly overestimate the threshold fluence at the longest pulse durations.

### 3.2.2  Pulse-duration dependence of the melting depth

The melting depth is defined as the maximum depth at which the combined energy in the electron and lattice systems exceeds the energy needed for the material to undergo heating and melting. Formally it can be written as

$$C_l T_{l,max} + \frac{C'_e}{2} T^2_{l,max} \geq \Delta H_m + C(T_m - T_0) \qquad (3.12)$$

where $\Delta H_m$ is the enthalpy of melting, $T_m$ is the melting temperature and $T_0$ is the initial temperature.

As can be seen from Fig. 3.6(b) the melting depth for copper at the threshold fluence increases dramatically as longer pulses are applied. The same three regions as before are seen. We observe a melting depth independent of pulse duration for pulses shorter than 1 ps (red dashed line in Fig. 3.6(b)), then a transition region and finally an increase proportional to $\tau^{0.51}$ for pulses longer than $\sim 40$ ps (green

dash-dotted line in Fig. 3.6(b)). Again a $\sqrt{\tau}$ dependence can be derived from approximate calculations, see e.g. Refs. [12] and [42]. The melting depth is observed to increase from 32 nm at 100 fs to more than 1 $\mu$m at 20 ns pulse duration.

A laser system for an application requiring a specific precision can thus be found from Fig. 3.6(b). If it is desired to have small heat affected regions, e.g. in order to maintain the native strength of a given material, it is seemingly necessary to employ ultra-short laser pulses.

## 3.3 Comparison with data

The experimental details are described in section 2.2. It should be noted, that with the applied spot size the assumption of a 1D model as discussed above is valid. In multi-shot ablation the absorptance changes as more pulses are applied, so we need to introduce an average absorptance to match the multi-shot experimental data to the single-shot theoretical simulation.

The values applied to match the data are $A_{multi}^{Cu} = 0.32$, $A_{multi}^{Ag} = 0.26$ and $A_{multi}^{W} = 0.80$. Note that the absorptance is the only adjustable parameter, and using these values, good agreement with the data is obtained over the entire fluence range, see Fig. 3.5. It should also be noted that introducing a fluence dependent absorptance (like $A_{low}$ and $A_{high}$ in chapter 2) could have improved the agreement between experiment and simulation, but we regard this as a more complicated and unnecessary procedure.

The role of ballistic electrons for heat transport has been discussed in the literature, see e.g. Refs. [31, 43]. The simplest way to include ballistic electrons is to modify the expression for the laser source term

$$Q = \frac{AI(t)e^{-2r^2/\omega^2}e^{-z/(\frac{1}{\alpha}+\lambda_{ball})}}{\frac{1}{\alpha}+\lambda_{ball}}, \tag{3.13}$$

where $\lambda_{ball}$ is ballistic electron penetration depth. It is seen that in this description only the deposition depth of the energy is changed. However this can also drastically change the threshold fluence. Figure 3.7 shows the effect of incorporating ballistic electrons into the model.

Since energy is carried into the deeper parts of the material, the threshold fluence is significantly higher as the energy density at the surface is decreased. It is seen that there is a much better agreement with the data, particularly in the low fluence regime, when ballistic electrons are included. It is however only of minor importance for transition metals as can also be seen in the case of tungsten in Fig. 3.5.
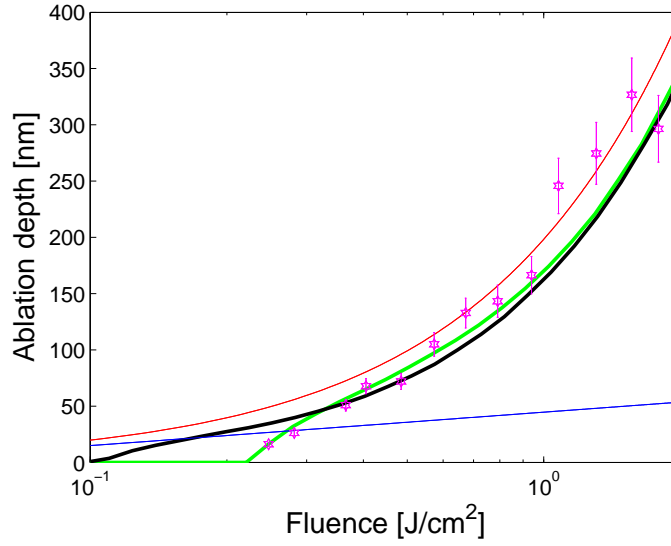
**Figure 3.7.** *The green line represents the TTM simulation with the inclusion of ballistic electrons. Much better agreement with the data, particularly in the low fluence regime, is observed. Legend as in Fig. 3.5.*

The value of the ballistic electron penetration depth is estimated as follows: The effective penetration depth can be found from the experimental data by making a fit of the low-fluence data points to the equation $L_\ell = \ell \cdot \ln \frac{F}{F_{th}}$, where $\ell$ is the effective penetration depth. The simulated penetration depth in the absence of ballistic electrons is found by fitting the simulated depths to the same equation. The ballistic electron penetration depth can then be found as the difference, i.e. $\lambda_{ball} = \ell_{exp} - \ell_{sim}$.

We find $\lambda_{ball}^{Cu} = 15 \pm 4$ nm, $\lambda_{ball}^{Ag} = 53 \pm 7$ nm and no signature of ballistic electrons for tungsten. These values should be compared to the optical penetration depths of 13 nm, 12 nm and 23 nm for copper, silver and tungsten, respectively. We emphasize that these values of the ballistic electron range in the noble metals must be incorporated in a description applying the TTM before an accurate prediction of the ablation rates can be made.

The values of the ballistic electron range should be of the same order as the electron mean free path, $\ell_{mfp} = v_F \cdot \tau_r$ where $v_F$ is the Fermi velocity and $\tau_r$ is the Drude relaxation time. The mean-free path is estimated from tabulated values in Ref. [44], assuming that the electrons travel through a sample, which is essentially at room temperature. The estimates are $\ell_{mfp}^{Cu} = 42$ nm and $\ell_{mfp}^{Ag} = 56$ nm, which

is seen to be in reasonable agreement with our values.

These values are somewhat smaller than the electron mean-free path reported in Ref. [31], where values of 70 nm and 142 nm for copper and silver are found. However, the specific characteristics of the sample may influence this range. For instance the thickness and particularly the crystallinity of the sample is important. The mean-free path is expected to be much longer in single-crystalline samples than in amorphous material.

## 3.4  Conclusion

We have experimentally measured the ablation rate at various fluences and compared these with computer simulations based on the two-temperature model. When incorporating ballistic electrons into the model, we find very good agreement between experiment and simulation. Both data and simulations seem to be consistent with a linear dependence at high fluence.

From the simulations, we also show that the threshold fluence and melting depth are constant for pulses shorter than 1 ps and increase as $\tau^{0.47}$ and $\tau^{0.51}$, respectively, for pulses longer than approximately 40 ps. The long-pulse behavior is in good agreement with approximate analytical calculations yielding a $\sqrt{\tau}$ dependence.

# CHAPTER 4

# Reflectance and ablation rate of samples undergoing femtosecond laser structuring

In this chapter the reflectance of a surface undergoing femtosecond laser ablation is studied and related to the varying ablation rate. An experimental setup capable of measuring the reflectance and ablation rate during laser structuring is presented, and the experimental data are compared to a model relating the reduction in reflectance to the evolution of ripples forming in the area of the laser spot. The model is shown to be consistent with the data, and provides information about the varying reflectance, scattering and absorptance of the sample undergoing structuring.

## 4.1   Introduction

The reflectance is the fraction of the incident electromagnetic power that is reflected at an interface. It is the square of the reflectivity, which is a measure of the fractional amplitude of the reflected electromagnetic field. As mentioned in chapter 2 the Fresnel reflectance is given by

$$R_f = \left| \frac{\tilde{n} - 1}{\tilde{n} + 1} \right|, \tag{4.1}$$

where $\tilde{n}$ is the complex refractive index.

One of the fundamental questions in the laser-material interaction is which reflectance the sample exhibits. It is quite obvious that the reflectance decreases after irradiation by multiple laser pulses, but a direct measurement of the reflectance *during* the ablation process is necessary to get a good understanding of the underlying physics.

## 4.2   On-the-fly depth profiling system

*In situ* measurement of the reflectance and hole depth can be performed with the setup shown in figure 4.1 [30, 45].

By means of a beam splitter, pulses from the laser system travel two separate ways before they meet again in the non-linear (BBO) crystal. The most intense overlap of the pulses at the crystal can easily be shown to be when 2/3 of the light is reflected. A R/T = 70/30 beam splitter is therefore applied in the setup.

The transmitted part is focused by a lens onto the sample subject to machining, while the reflected part goes into a delay arm. When adjusting the variable delay arm to be the same length as the sample arm, the overlap of the two pulses will be in the middle of the crystal. When the pulses strike the sample surface and start ablating, the sample arm will become longer and the overlap at the crystal thereby change, see the inset of Fig. 4.1.

A second harmonic signal ($\sim$400 nm) in the forward direction is thus seen and the laser drilling process can be observed as a blue line moving upwards as the sample undergoes ablation. A CCD camera connected to a frame-grabber card is recording the process, yielding the intensity in each pixel as a function of time. Since the second harmonic signal is horizontal, the rows of the CCD are summed over all the columns to find the intensity in each of the 488 individual rows. In section 4.5 the rows shall be denoted "pixel number" since it corresponds to the pixel number in the vertical direction.
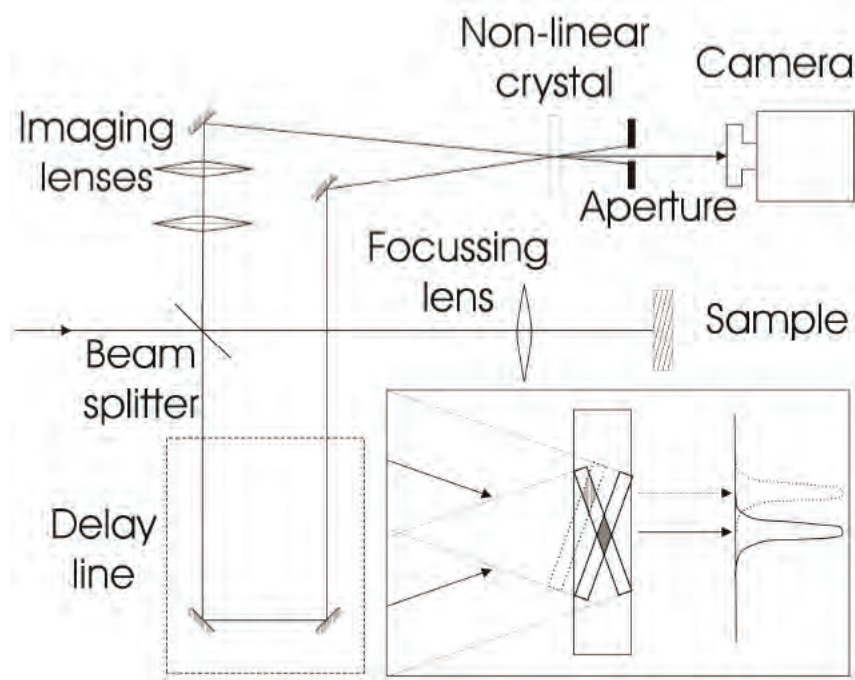
**Figure 4.1.** *Setup for* in situ *measurement of hole depth and reflectance. Details are described in the text.*

A requisite for using this technique is that the pulses are ultra short. 100 fs pulses have a spatial extent of approximately 30 $\mu$m, while nanosecond pulses will be in the range of several centimeters, and thus smear out the overlap signal. The spatial resolution obtained with 100 fs pulses is in the order of a few micrometers.

The information gained from this setup is firstly the time evolution of the hole, i.e. the time varying ablation rate, and secondly the time varying reflectance. The backscattered light is collected with the same lens that is used to focus light onto the sample, and by measuring the intensity of this light, a direct measure of the specular reflectance is acquired. Normalizing to the initial reflectance (often the Fresnel reflectance) an absolute measure of the reflectance as a function of time is obtained.

It should be mentioned that the camera typically operates at a frame rate of approximately 10 fps, which means that the individual data points are an average over approximately 100 laser pulses, when a repetition rate of 1 kHz is applied. It is possible to average over a fewer number of pulses simply by reducing the repetition rate of the laser to e.g. 100 Hz, but this of course reduces the intensity of the mixing signal.
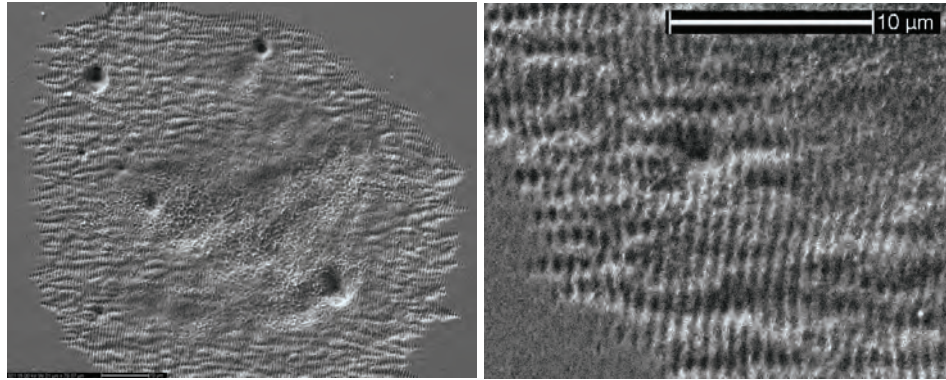
**Figure 4.2.** *SEM image of a copper surface after 1000 pulses at a fluence slightly above the damage threshold. The scale bar in the close up is 10 $\mu$m.*

The direct applicability of precisely controlling the depth of the holes should be noted. Since reproducibility is a key parameter for many applications, the ability to follow the ablation during the drilling process is invaluable. Providing a feedback mechanism to the setup, the ablation can be ceased at the exact desired hole depth for a large array of holes.

## 4.3   Incubation and ripples

As discussed in chapter 2 it is a well known phenomenon that the apparent threshold for ablation with pulsed lasers decreases after irradiation by multiple pulses. This phenomenon is called incubation. The precise mechanism behind the observed incubation effect is, however, still an open question.

Originally it was proposed that the incubational behavior for metals was due to the accumulation of plastic deformations, resulting from laser-induced thermal stress [46]. However, Lausten *et al.* [45] suggest that incubation may also be due to the increased absorption arising from roughening of the surface in multi-shot measurements. Figure 4.2 shows a SEM image of a polished Cu surface after irradiation by 1000 laser pulses at a fluence slightly above the damage (melting) threshold.

It is clearly seen that a ripple pattern has appeared and that the periodicity of the ripples is of the order of the laser wavelength. A thorough discussion of ripples is presented in [12], and many interesting aspects are given in the articles by the research group of Guo [47–52].

In the case of metals, the ripple pattern is almost always perpendicular to the

direction of the polarization of the incoming light. When using circularly polarized light no ripples are observed. Two different mechanisms for ripple generation need to be mentioned.

Firstly the ripples can be generated from the interference between a surface scattered wave from the initial part of the pulse and the remaining part of the pulse. The spacing of these ripples is given by the equations 4.2 and 4.3 [12]

$$\Lambda = \frac{\lambda}{1 \pm \sin\theta} \tag{4.2}$$

$$\Lambda = \frac{\lambda}{\cos\theta} \tag{4.3}$$

depending on the direction of the scattered wave relative to the surface corrugation. $\lambda$ is the laser wavelength and $\theta$ is the angle of incidence. In an experimental setup where the laser beam strikes the surface at normal incidence both equations are seen to give the laser wavelength.

The incoming light can be scattered by microscopic surface roughness, defects, spatial variations in the dielectric constant, etc. Due to the interference pattern, the damage threshold can be periodically exceeded, so that the material melts and resolidifies in the given pattern. The periodic structures on the surface will then act as a grating, leading to more of the incoming light being scattered and thereby more energy being coupled into the sample.

There will be constructive interference in the "valleys" and destructive interference on the "hills", and this positive feedback mechanism will cause the growth of ripples with a spacing of the laser wavelength. Because of local field enhancement on the hills this otherwise self enhancing process ends at some point where an equilibrium ripple height is reached.

The other mechanism producing ripples is interference between the incoming light and surface plasmons. Surface plasmons are fluctuations in the electron density at the interface between two materials (metal-air in the present case). When surface plasmons couple with photons, the resulting quasi-particle is called a surface plasmon polariton (SPP). They can be thought of as particles traveling along the surface due to an oscillating electric field produced by surface electrons oscillating in phase normal to the surface.

The SPP's will decay over a short distance whereupon the energy is converted into phonons. This means that an additional incoupling mechanism for the light is provided. Excitation of SPP's has been experimentally observed as sharp dips in the reflectance, when the conditions for excitation are met [53].

At normal incidence the ripple spacing due to SPP's is given by [12]

$$\Lambda = \frac{\lambda}{n_{SPP}} \tag{4.4}$$

where $n_{SPP} = \sqrt{\frac{|\epsilon'|}{|\epsilon'|-1}}$ is the real part of the effective index of refraction for the air-metal interface and $\epsilon'$ is the real part of the dielectric constant. A requirement for the excitation of SPP's is that the real part of the dielectric constant of the metal is smaller than $-1$. As the complex dielectric constant is given by $\epsilon = (n + \imath k)^2$ the condition may be written as

$$\epsilon_{real} = n^2 - k^2 < -1. \tag{4.5}$$

Both $n$ and $k$ are frequency dependent so SPP's may be supported only at certain wavelengths. In the region of 800 nm metals like Al, Ag and Cu have $\epsilon_{real} < -1$ while Mo and W have positive $\epsilon_{real}$ and thereby do not support SPP's. SPP's cannot be excited at normal incidence on a smooth metal surface, which means that the surface needs to have some roughness, which can scatter the incoming light, so that the polarization of the light is perpendicular to the surface thereby initiating the electronic oscillations.

## 4.4   Model

As discussed in section 2.3.2.1 the ablation rate in the low-fluence regime is typically expressed as $L_{low} = \ell \cdot \ln\left(\frac{F}{F_{th}}\right)$. Operating very close to threshold the effective penetration depth can be approximated by the optical penetration depth $1/\alpha$. Taking into account that only the incoupled fluence affects the material, the ablation rate may be written as

$$L_n = max\left\{\frac{1}{\alpha} \cdot \ln\left(\frac{A_{n-1}F}{A_{init}F_{th}}\right); 0\right\}. \tag{4.6}$$

$L_n$ is the amount of material removed by the n'th pulse, $A_{n-1}$ is the absorptance after (n-1) pulses, $A_{init}$ is the initial absorptance which is typically given by (1-$R_{Fresnel}$) and $F_{th}$ is the threshold fluence given by $F_{th} = \frac{\Delta H_{vap}}{\alpha A_{init}}$. The equation also takes into account that for incoupled fluences smaller than the incoupled threshold fluence no material is removed. The depth of the ablated hole after n pulses is thus

$$d_n = d_{n-1} + L_n \tag{4.7}$$

Incubation can be observed as an increase in ablation rate as more pulses are applied. It is seen that incubation in the present model is caused solely by an increase in the absorptance, A, with the number of applied pulses.

The present model describes the increase in absorptance in relation to the evolution of ripples forming in the area of the laser spot. Previous models have described the dynamics of ripple-formation but without relating it to the process of ablation [54,55]. It should be emphasized that the ripple height is not actually measured in the present experiment. It is merely a parameter in the modeling which makes the reflectance decrease.

The basic idea is that each of the initial laser pulses will increase the ripple height by a small amount $\delta h$ towards the final height $h_{final}$. As mentioned in section 4.3 the ripples will grow to a finite height where the positive feedback mechanism is balanced by the local field enhancement on the "hills".

Assuming that $\delta h$ is linearly dependent on the difference between the current and the final ripple height times the ratio between the incoupled fluence and the threshold fluence, Eq. (4.8) expresses the ripple height after n pulses

$$h_n = \phi \frac{A_{n-1}}{A_{init}} \frac{F}{F_{th}} (h_{final} - h_{n-1}) + h_{n-1} \qquad (4.8)$$

where $\phi$ is a constant feedback parameter. The reflectance after the n'th laser pulse is correspondingly assumed to be given by Eq. (4.9)

$$R_n = R_{init} - \frac{h_n}{h_{final}} (R_{init} - R_{final}) \qquad (4.9)$$

where $R_{init}$ is the reflectance before the first laser pulse (approximately equal to the Fresnel reflectance for a polished surface), and $R_{final}$ is the reflectance that is reached when the ripple height settles at its final value.

Since R only accounts for specular reflection, a scattering term must be introduced. This is done by assuming that the scattering increases at the same rate at which the reflectance decreases, i.e.

$$S_n = k(R_{init} - R_n), \qquad (4.10)$$

where $k$ is a constant between 0 and 1. Finally, the absorptance is found as the part of the light that is not reflected or scattered

$$A_n = 1 - R_n - S_n = A_{init} + (1-k)(R_{init} - R_n). \qquad (4.11)$$

It is seen that $k = 0$ indicates no effect of scattering while 1 indicates that the reduction in reflectance translates directly to an increase in scattering without

increasing the absorptance.

Inserting Eq. (4.9) into Eq. (4.11) which is then inserted into Eq. (4.8) yields an expression that can be numerically propagated to find the ripple height as a function of the applied number of pulses. The reflectance is now found from Eq. (4.9) and can be compared with experimental data. The absorptance can thus be found and inserted into Eq. (4.6), whereby the simulated ablation rate is found.

## 4.5   Results and discussion

Measurements have been performed on a polished copper surface with the system described in section 4.2. The laser was running at a repetition rate of 300 Hz and the sample was positioned 1 mm behind the focus yielding a slightly elliptical beam with a major and a minor spot size of 106 $\mu$m and 91 $\mu$m, respectively.

A fluence of 1.37 J/cm$^2$ corresponding to an incoupled fluence of 55.0 mJ/cm$^2$ (equal to the theoretical threshold fluence) was applied. The raw data can be seen in Fig. 4.3 where the intensity of the backscattered light is plotted as a function of the pixel number (row on the CCD) and the number of applied pulses.

It is seen that the intensity decreases dramatically during the first 1000 pulses. Two different peaks are observed: One decreases in pixel number from the initial $\sim$ 320 to the final $\sim$ 200. This is the light reflected from the bottom of the hole. The other peak is fairly constant at $\sim$ 320. This is the light reflected from the surface. Since the reflectance of the central part of the holes rapidly decreases, the constant signal originates from the wings of the Gaussian intensity distribution which still encounters a smooth surface and is therefore strongly reflected.

To find the position and intensity of the ablation-peak a fit was made to a Gaussian intensity distribution for each frame. The fits (red curves) along with the experimental data (blue circles) are shown in Fig. 4.4 for 3 different numbers of applied pulses.

The position of the peak provides information about the depth of the hole and the area under the curve provides information about the reflectance. A calibration is made to convert the pixel number into a position relative to the surface and the depth can thus be found as a function of the number of applied pulses. The purple squares in Fig. 4.5 represents the depth found in this way.

When the area under the Gaussian fit curve is normalized to the Fresnel reflectance it is a direct measure of the reflectance of the sample after a varying number of applied pulses. This is shown as the blue circles in Fig. 4.6.

The reflectance is fitted to Eq. (4.9) with the simulated ripple height inserted. An initial value of $k$ is inserted while the fitting parameters are a scaling factor and
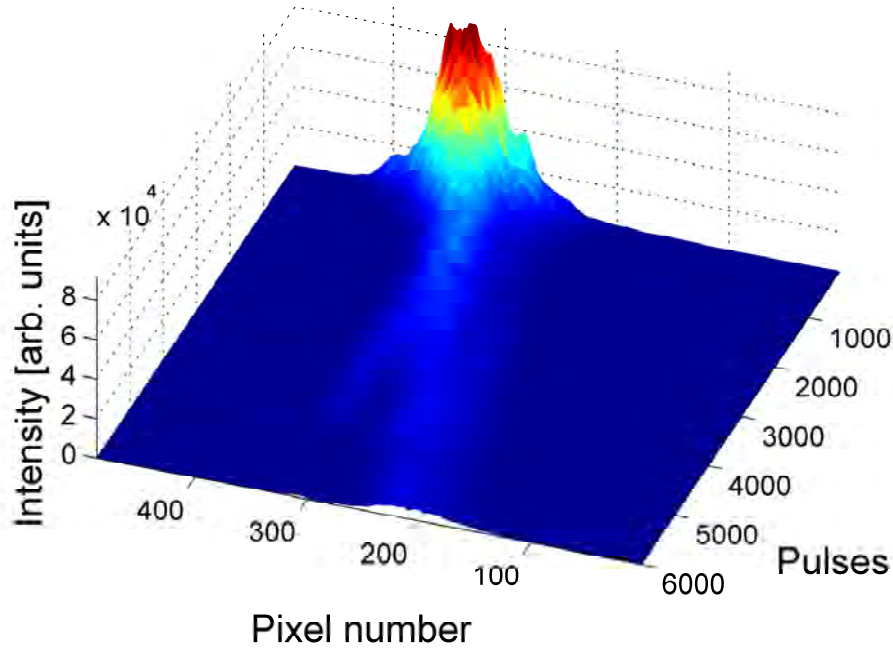
**Figure 4.3.** *The intensity of the backscattered light during the ablation process as a function of the pixel number and the number of applied pulses. An incoupled fluence of 55.0 mJ/cm$^2$ was applied.*

$R_{final}$. The depth is then fitted to Eq. (4.7) with the expression for the reflectance found from the previous fit inserted. In the depth-fit an offset and the factor $k$ are the fitting parameters. This value of k found from the depth-fit must now be inserted in the fit for the reflectance and these two fits are iteratively performed until the value of the fitting parameter agrees with the inserted value.

The fits provide the reflectance, scattering and absorptance as a function of the applied number of pulses, see Fig. 4.7.

The value obtained for the final reflectance is $R_{final} = 0.084 \pm 0.003$. This means that the reflectance decreases from 96% to 8% during the ablation process. From the final value of $k$ the final absorptance is found from Eq. (4.11) to be $A_{final} = 0.054 \pm 0.004\%$. A very small increase in absorptance (which is initially 0.040) is thus observed whereas more than 86% of the laser power is lost due to scattering in the final state.

The variance between $A_{low} = 0.37$ found in chapter 2 and $A_{final} = 0.054$ found here should be noted. As shown in Fig. 2.4, the ablation rate, and thereby
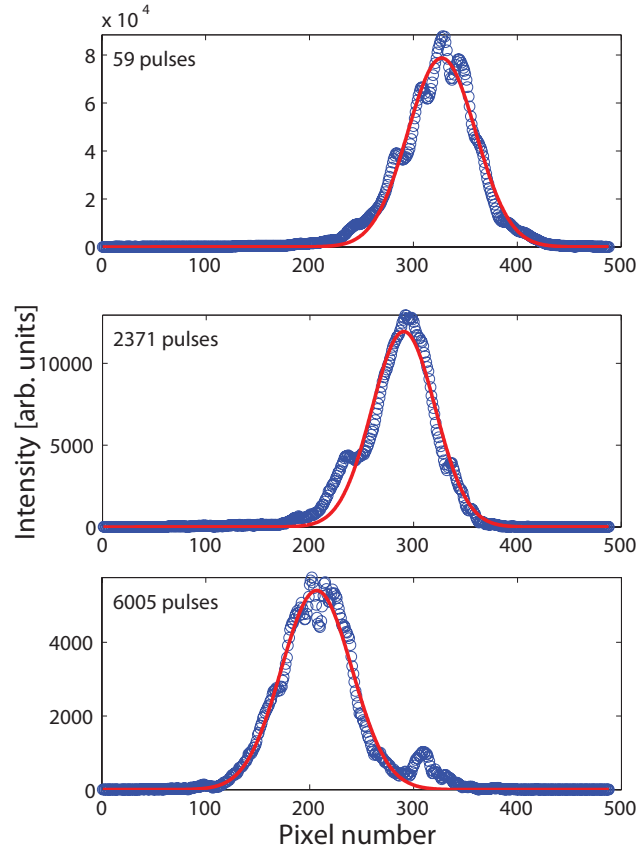
**Figure 4.4.** *The intensity of the backscattered light during the ablation process as a function of the pixel number for different numbers of applied pulses. The blue points are the measured intensity in each row of the CCD and the red curve represents a fit to a Gaussian intensity distribution.*

the absorptance, drops when more than $\sim 100$ pulses are applied. However, this trend cannot be directly translated to the present case since a different laser spot size is applied but it can still explain some of the discrepancy. Also, operating at a fluence just above the threshold could be responsible for a decrease in absorptance compared to the scenario in chapter 2. It could be interesting to measure the ablation rate and reflectance on a pulse to pulse basis during the first hundred pulses. This would, however, require a better camera since the signal in the present setup is to faint when operating at very low repetition rates.
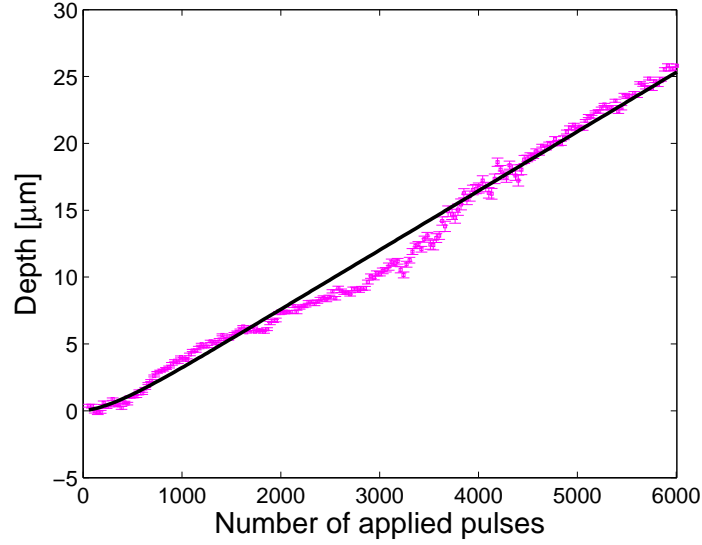
**Figure 4.5.** *The depth of the ablated hole as a function of the applied number of pulses. The purple squares represent the experimental data and the black solid line is a least square fit to the model as described in the text. The error bars represent the 1σ standard deviation found when performing the fit to a Gaussian function.*

## 4.6  Conclusion

An experimental setup has been described which can simultaneously measure the reflectance of a surface undergoing ablation and the depth of the hole being ablated. This is done *in situ* and can thus provide information about the dynamics of the ablation process during the structuring.

A model is presented in which the reduction in reflectance is related to the formation of ripples in the area of the laser spot. In this model incubation is observed as an increase in the ablation rate as a larger number of pulses are applied.

The model is shown to be consistent with the experimental data using only a few fitting parameters. From the fits the fraction of the laser power going to reflectance, scattering and absorptance is found as a function of the applied number of pulses. The reflectance is observed to decrease from 96% to 8% within a few thousand pulses, while the absorptance only increases from 4% to 5%. This means that more than 86% of the incoming laser light is lost due to scattering.
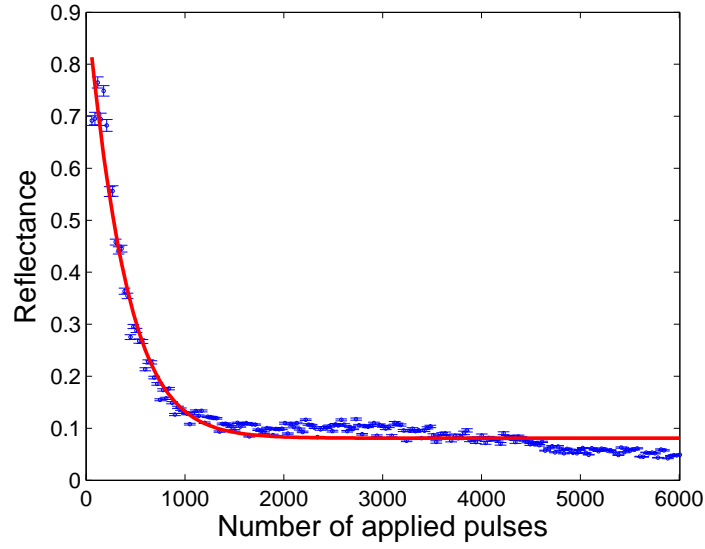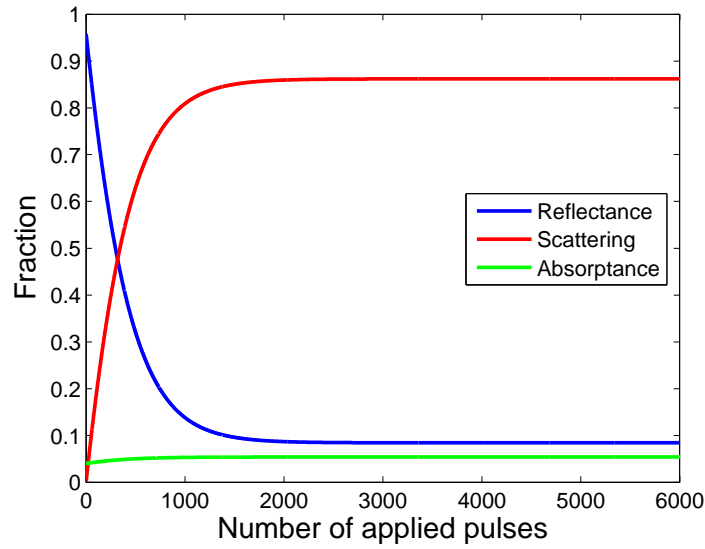
**Figure 4.6.** *The reflectance versus the applied number of laser pulses. The blue circles represent experimental data and the red solid line is a least square fit to the model as described in the text. The error bars represent the $1\sigma$ standard deviation found when performing the fit to a Gaussian function.*



**Figure 4.7.** *Reflectance, scattering and absorptance (obtained from fits to the experimental reflectance and hole depth) as a function of the applied number of pulses. Only a slight increase in absorptance is observed.*

# Part II

# MICRO-MECHANICAL INTERLOCKING

# CHAPTER 5

# Optimizing material removal by nanosecond laser structuring

This chapter describes ablation experiments performed on stainless steel samples with a nanosecond laser system. The purpose is to examine how the ablated surface structures depend on the applied laser parameters and the pulse irradiation strategy. Precise knowledge of the surface topography is necessary in order to achieve micro-mechanical interlocking (MMI), which is the topic of chapter 6.

As mentioned in the introduction, nanosecond lasers do more damage to the surrounding material but have a higher throughput than femtosecond lasers and are thereby more industrial friendly. Since MMI aims to be an industrial technique nanosecond laser systems are at the moment the preferred choice.

This chapter is based on the article "Laser structuring of metal surfaces: Micro-mechanical interlocking", Applied Surface Science **255** (2009) 5591 [4].

## 5.1   Introduction

To achieve MMI the properties of material joints must be well understood. These properties are determined by several different parameters ranging from the macroscopic level over the nanoscale ultimately down to the individual molecular bonds. Precise control of the surface topography is thus of major importance for tailoring the characteristics of specific material interconnects. Laser micro-structuring of surfaces opens up for a broad range of applications, which have been demonstrated to be affected by the detailed structure of the surface (see, e.g., Ref. [21]). For instance, it has recently been demonstrated that laser-structured titanium surfaces exhibit an increase in the adhesive bond strength [56]. The present state-of-the-art in composite materials is typically based on advanced chemical bonding, and to a much less extent the use of designed surface topography. These techniques may, however, often provide neither bonding that exhibits sufficiently high mechanical strength nor a high tolerance to temperature changes - properties, which are essential for many industrially relevant situations.

## 5.2   Experimental

The experiments described in chapter 5, 6, 7 and 8 are carried out using a TruMicro 3040 from TRUMPF [5]. The specifications are listed in the table. Figure 5.1 shows the pulse energy (circles in connection with the left y-axis) and output power (squares in connection with the right y-axis) as a function of the repetition rate. The power is seen to be fairly constant at 40 W over the entire repetition rate range except at 8 kHz.

| $\lambda$ [nm] | $P_{ave}$ [W] | $\tau$ [ns] | $E_p$ [mJ] | Rep. [kHz] |
|---|---|---|---|---|
| 1047 | 40 | 25 - 120 | $< 4$ | 8 - 70 |

For a detailed discussion of nanosecond laser ablation see Ref. [12]. A commercial 2D scan head is mounted to move the focal point of the laser beam around in the plane of the sample. The experiments presented here are performed with an $f = 254$ mm lens giving a minimum spot size $\omega_0 = 47$ $\mu$m leading to a peak intensity of $\sim 300$ MW/cm$^2$. Using this lens provides a square working field of 180x180 mm.

Ablation studies were carried out on six different types of steel (1.4301, 1.4362, 1.4401, 1,4462, 1.4509 and 1.4539). The results were very similar, and only those
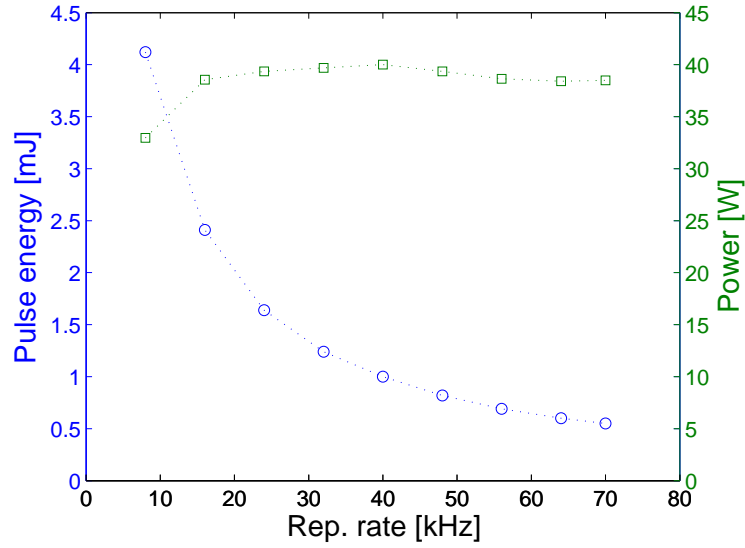
**Figure 5.1.** *Pulse energy (circles in connection with the left y-axis) and output power (squares in connection with the right y-axis) as a function of the repetition rate.*

of type 1.4401 shall be presented. After laser structuring, the ablated areas were investigated using a scanning electron microscope (SEM) and selected samples were polished in order to get a side view of the holes. The diameter of the holes could in many cases be found from the SEM pictures but in some cases the recast material blocked the hole, making it necessary to evaluate the diameter from the side-view pictures. The depth of the holes was found from light microscopy by focusing first on the surface and then on the bottom of the hole. This method is accurate within a few micrometers.

## 5.3   Results and discussion

An important parameter for the laser processing is the pulse energy. Fig. 5.2 shows SEM images of holes made with two different pulse energies. The laser is maintaining an almost constant average output power as we change the pulse energy, which means that changing from 1.0 mJ/pulse to 0.69 mJ/pulse also implies an increase in repetition rate from 40 kHz to 56 kHz. Keeping the irradiation time per hole fixed (at 1.25 ms in the present case) a lower pulse energy is thus equivalent to a larger number of pulses. It is therefore not obvious what will be the optimum
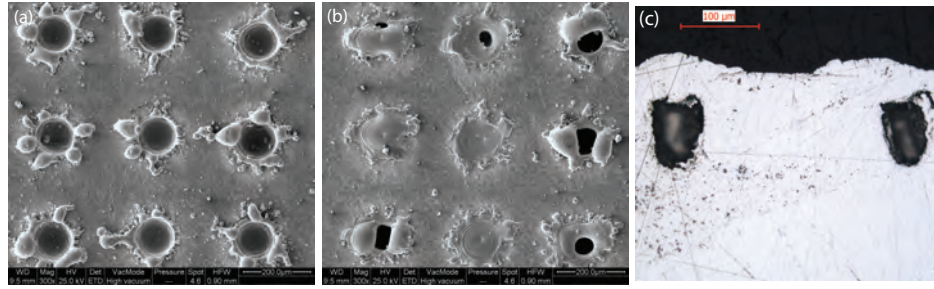
**Figure 5.2.** *(a) Type 1.4401 steel after irradiation by 50 pulses at a pulse energy of 1.0 mJ (corresponding to 29 $J/cm^2$) and a repetition rate of 40 kHz and (b) after irradiation by 70 pulses at a pulse energy of 0.69 mJ (corresponding to 20 $J/cm^2$) and a repetition rate of 56 kHz. Production time per hole is 1.25 ms in both cases. (c) shows a side view of the 56-kHz holes after polishing. The separation between the holes is 300 $\mu$m.*

pulse energy for micro machining.

At 56 kHz it is seen that the recast material is in some cases blocking the hole. The side view of the holes at 56 kHz confirms that there is a cavity underneath the recast. The depth of the covered holes is roughly the same as the depth of the holes where recast does not cover the holes. This means that the covering is happening in the end of the drilling process or probably even after the process is over.

The same tendency applies for even higher repetition rates, which indicates that surface structuring for efficient MMI must be undertaken at repetition rates below 56 kHz unless special care is taken. One thing that can be done to avoid sealing the holes is to allow the material to cool off between laser pulses by moving on to another hole, thus shooting an array of holes, returning to each hole a number of times instead of applying all the pulses in a single burst. Fig. 5.3 shows arrays of holes with 150 $\mu$m spacing. In panel (a), the drilling of each hole is finished before moving on, while in the situation corresponding to panel (b) each hole in the 20x20 array is ablated by 1 pulse 50 times.

Holes drilled with 50x1 pulse are clearly more separated and the recast is building up burr locally around the holes. However, both diameter and depth has decreased significantly when allowing the material to cool off, see Fig. 5.4. Furthermore, the production time of the 50x1 holes is 11 times longer than the 1x50 holes, since the scan head must steer the beam to each hole 50 times.

These results indicate that heating of the sample plays a crucial role in the ablation process. Another indication of the heat dependence is manifested by the fact that when applying a distance between the holes of 150 $\mu m$, the holes become ap-
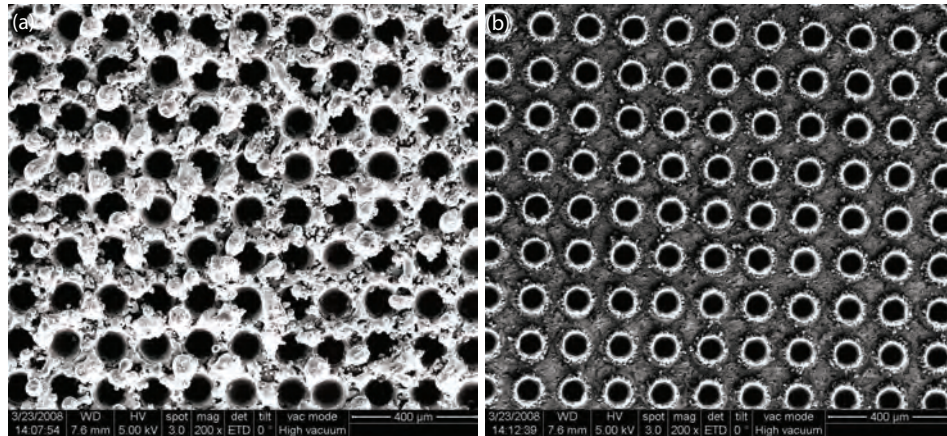
**Figure 5.3.** *Type 1.4401 steel after irradiation by two different sequences of 50 pulses at a pulse energy of 1.0 mJ (29 $J/cm^2$), see discussion in text. In panel (a), the array of holes is structured according to the burst mode, i.e. 1x50 pulses, whereas the array in panel (b) is structured according to the sequential mode, i.e. 50x1 pulse. The separation between the holes is 150 $\mu$m.*
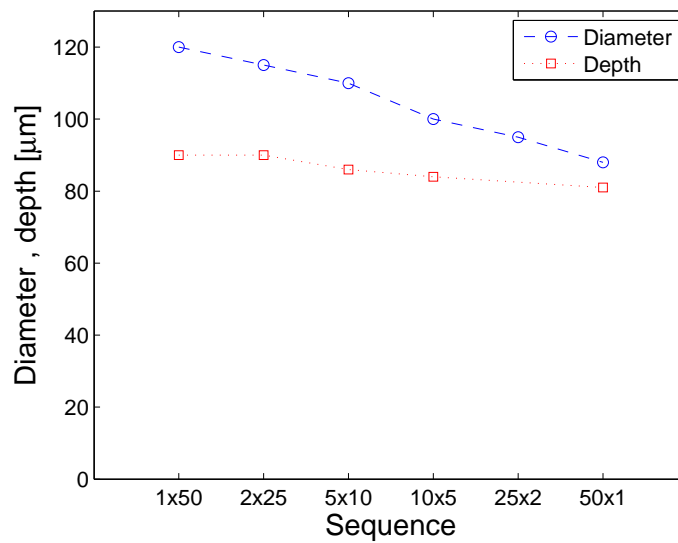


**Figure 5.4.** *The ablated hole diameter and hole depth as a function of the sequence with which the holes were made. A fluence of 29 $J/cm^2$ was applied. The blue circles represent diameters while the red squares represent depths.*
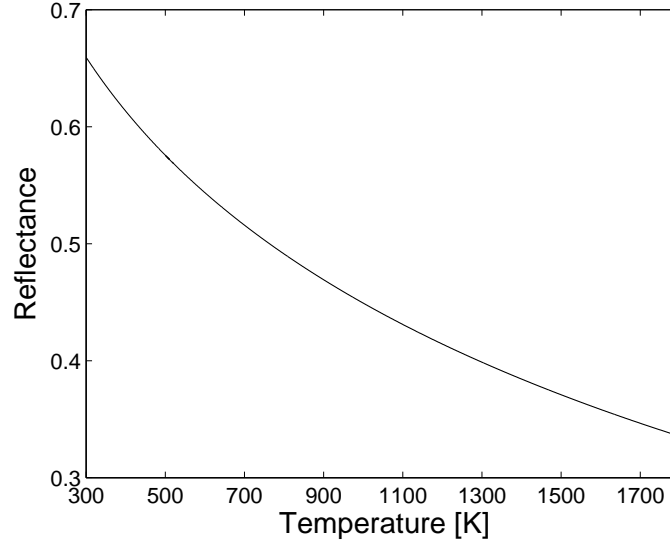
**Figure 5.5.** *Reflectance of iron as a function of temperature - calculated from Eq. (5.1).*

proximately 20 % deeper than if the spacing is 300 $\mu m$. Furthermore, the thickness of the sample seems to be of importance: With a thin sample, the material in and around the hole will become hotter, resulting in a larger ablation rate.

Fig. 5.5 shows a calculation of the reflectance of iron as a function of temperature at the laser wavelength, i.e. 1047 nm. The Fresnel reflectance at normal incidence is given by

$$R(\lambda, T) = \left| \frac{1 - \tilde{n}(\lambda, T)}{1 + \tilde{n}(\lambda, T)} \right|^2, \tag{5.1}$$

where $\tilde{n}(\lambda, T)$ is the complex refractive index of the material on which the laser beam impinges and the refractive index of air has been taken equal to one. The temperature dependence of $\tilde{n}$ is found from the dielectric function since $\tilde{n}^2(T) = \epsilon(T)$. The contribution to the dielectric function from free electrons is described by the Drude model,

$$\epsilon = 1 - \frac{Ne^2}{\epsilon_0 m} \frac{f}{\omega^2 + \imath \gamma \omega}, \tag{5.2}$$

where $N$ is the atom density, $e$ the elementary charge, $f$ the oscillator strength and $\gamma$ the collision frequency. We assume that the main part of the temperature dependence is carried in the $\gamma$ factor, which increases with temperature since higher
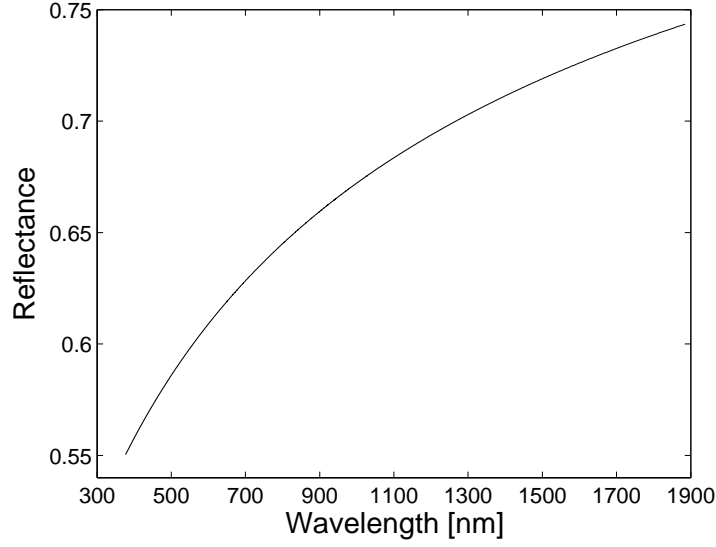
**Figure 5.6.** *Reflectance of iron as a function of wavelength - calculated from Eq. (5.1).*

temperature yields more collisions. The real and imaginary parts of the complex refractive index of iron can be found in the literature [26, 57], and we find that the dielectric function in the vicinity of the laser wavelength can be reasonably well approximated by the Drude expression, Eq. (5.2). The fit yields the value of $\gamma$ at room temperature. In the temperature range relevant for the present discussion, the collision rate is dominated by electron-phonon collisions, which means that a linear dependence of collision rate on temperature may be expected. Taking the collision frequency to be zero at 0 K, the value of $\gamma$ at all temperatures can be estimated. The temperature dependence of $\epsilon$ is then known and the temperature dependence of the reflectance can be calculated.

As it can be seen from Fig. 5.5, the 20 % increase in hole depth for the closely-spaced holes can readily be explained by an increase in the sample temperature of $\sim$200 degrees, since this increases the incoupled energy, $(1 - R)$, by $\sim$20 %.

Also the wavelength dependence of the reflectance can be found from Eq. (5.1), see Fig. 5.6

For instance, at 349 nm (frequency tripling) we see a 14 % better absorption than at 1047 nm. However, since the conversion efficiency to the third harmonics is usually only a few tens of percent, the calculation indicates that for steel, the highest material-removal efficiency is obtained by applying the fundamental laser
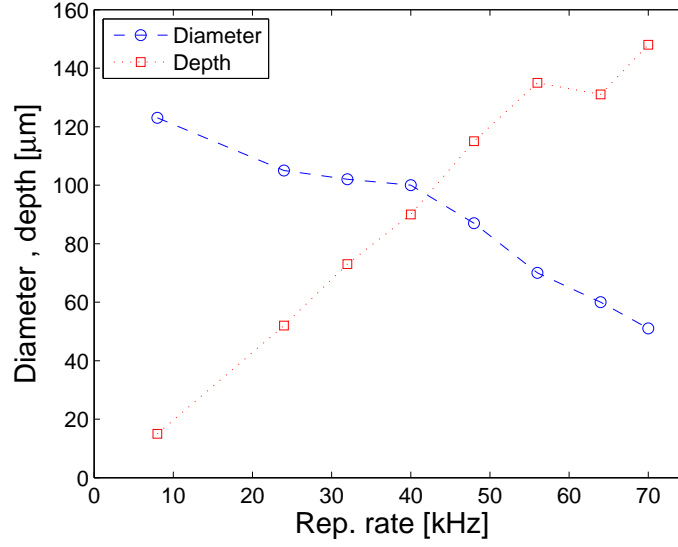
**Figure 5.7.** *The ablated hole diameter and hole depth as a function of laser repetition rate. The blue circles represent diameter while the red squares represent depth.*

frequency.

Since production time is a big issue, it is instructive to find the repetition rate at which the material removal rate is at its maximum. Keeping the irradiation time per hole fixed, the diameter decreases, while the hole depth increases as the repetition rate is increased, see Fig. 5.7. This is also expected since an increase in repetition rate yields a larger number of pulses but with a lower energy.

Assuming the removed volume to be given by $V = \pi r^2 h$ (where r is the radius of the hole and h is the depth) it turns out that there is a maximum around 40 kHz, see Fig. 5.8. At this repetition rate the laser removes $\sim 0.6$ mm$^3$/s. Material removal rates of this order is a requisite for large area surface structuring.

This shows that maximum efficiency of the laser light is obtained by operating close to 40 kHz. The output power from the laser is slightly higher around 40 kHz than for higher and lower repetition rates, but not enough to account for the observed ablation rate maximum.

It is seen from Fig. 5.9 that the hole depth increases approximately linearly with the number of applied pulses, which in the simplest description is reasonable. Since the Rayleigh range, for the present optical setup, is on the millimeter scale, much larger than the hole depth, the change in the laser spot size is negligible. On
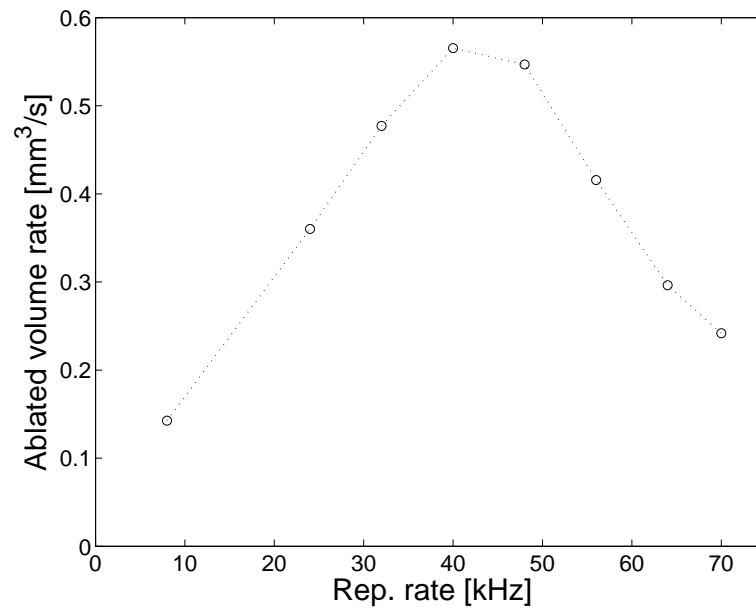
**Figure 5.8.** *Ablated volume rate as a function of laser repetition rate. The maximum material removal rate is reached around 40 kHz.*
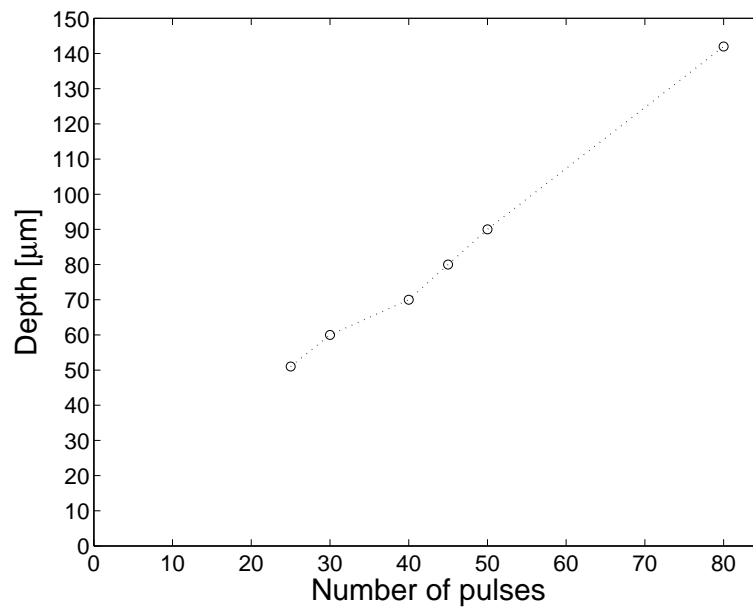


**Figure 5.9.** *Ablated hole depth as a function of the number of applied pulses. A fluence of $29\ J/cm^2$ was applied.*

the other hand, effects like heat propagation and changes in reflectance would give rise to a more complex dependence on the number of pulses. A linear fit to the data in Fig. 5.9 will give a positive offset of approximately 8 $\mu m$. This indicates that the ablation rate is somewhat higher during the first few pulses and then settles at a constant value at least until pulse number 80. The relatively linear behavior shows that the aforementioned effects, which are significant for deep holes, play a relatively small role in the present case, probably because the holes only have an aspect ratio of ~1.

All the different types of steel exhibit more or less the same tendencies. Measurements on Cu showed approximately the same depth/diameters for similar laser parameters, although the effects of allowing the sample to cool down seem to be absent.

## 5.4   Conclusion

It was demonstrated that at optimized laser-processing parameters, a high-average-power nanosecond laser is able to undertake precise micro-structuring of large surface areas with volume removal rates approaching 1 mm$^3$/s. This opens the possibility of applying a laser with its high flexibility, precision and reliability for several new application areas of surface texturing such as micro-mechanical interlocking, tribology, anti-fouling, biocompatibility, etc. Furthermore it has been demonstrated, both theoretically and experimentally, that the temperature of the sample plays a significant role in the ablation process.

# CHAPTER 6

# Micro-Mechanical Interlocking by laser surface structuring

In this chapter micro-mechanical interlocking (MMI) will be described. Laser surface structuring provides the ability to generate new strong composite materials by employing MMI. In this chapter, recent results from the optimization of material interlocking properties by laser-based surface micro-structuring are reported. The laser-based structuring provides much flexibility in the geometry of the interface, and a high strength is ensured by directly injection molding a plastic into the laser-structured surface. The dependence of the mechanical strength of the joint on the exact laser generated surface morphology is investigated. It is shown that appropriate surface structuring can increase the bonding strength by several orders of magnitude, yielding interlocking of very high mechanical stability.

This chapter is based on the article "Ultra-high-strength micro-mechanical interlocking by injection molding into laser-structured surfaces", International Journal of Adhesion and Adhesives **30** (2010) 485 [58].
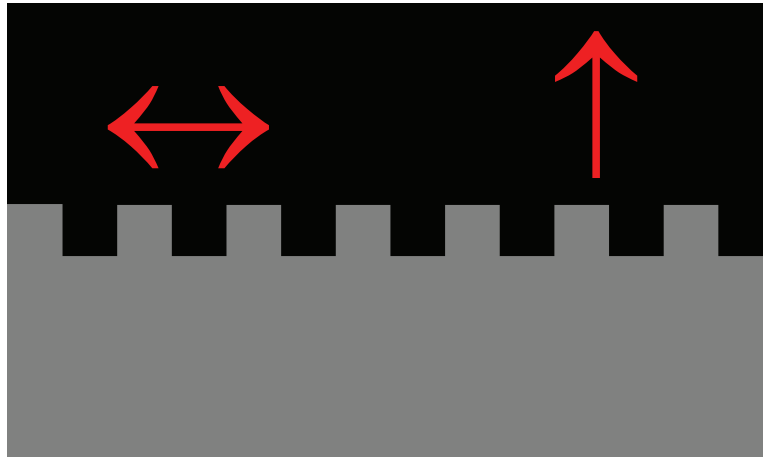
**Figure 6.1.** *Simple figure sketching the principle of MMI. In our case gray represents metal and black represents plastic.*

## 6.1   Introduction

The topography of a surface can to a great extent be controlled by laser structuring. Hereby the adhesive behavior of the surface can be governed and interlocking of different materials can be achieved. For an overview paper discussing laser structuring of surfaces for adhesion between a number of different materials, see Ref. [59].

Figure 6.1 shows the principle of MMI. By having a roughened surface the materials can obviously better stick together. The focus of this chapter will be on the *shear strength* of the interlocked samples (horizontal double-arrow) which is clearly better than the *normal strength* (vertical arrow) which will be discussed in chapter 7.

## 6.2   Materials and methods

The laser used for the micro-structuring is described in section 5.2. As discussed in section 5.3 the maximum material removal rate is found to be at 40 kHz / 1 mJ. Therefore a pulse energy of 1 mJ at a repetition rate of 40 kHz was chosen for all the experiments regarding MMI. At this repetition rate the pulse duration is approximately 90 ns. As in chapter 5 the laser light is focused onto the sample using an $f = 254$ mm lens giving a focused spot size of 47 $\mu$m leading to a peak intensity of $\sim 300$ MW/cm$^2$.
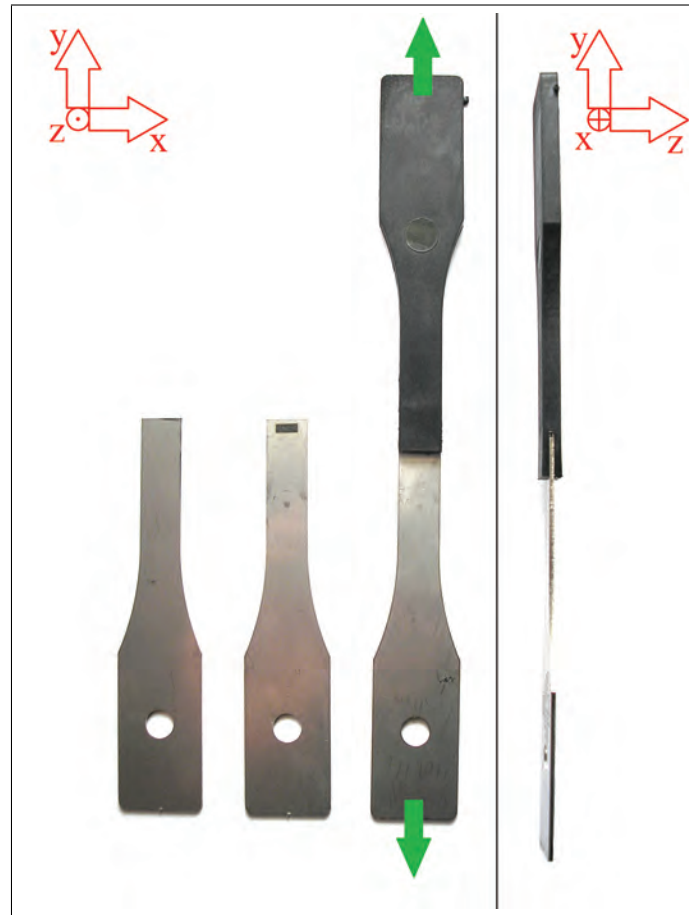
**Figure 6.2.** *From left to right: An unstructured metal test bar, a laser structured metal test bar, a laser structured metal test bar after injection molding of the plastic part and the joint part seen from the side. The geometry is described in the text. To find the strength of the joint load is applied in the $\pm$ y-direction as indicated by the green arrows.*

In this study stainless steel type DIN 1.4301 and plastic type Fortron MT9141L4 polyphenylene sulfide (PPS) containing 40 % glass fibres are applied. As previously mentioned, six different types of steel have been tested, but all gave the same surface morphologies at given laser treatments, so type DIN 1.4301 was chosen since it represents a very general type of stainless steel. Also, PPS was chosen as it is a widely used type of polymer.

The dimensions of the test sample are in accordance to the ISO 527 standard with slight modifications: The length (y-direction in Fig. 6.2) of the steel bar is
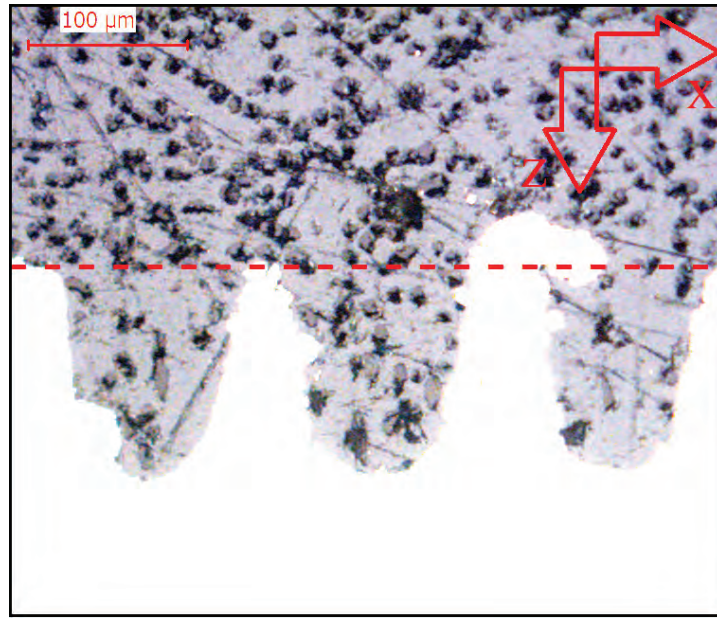
**Figure 6.3.** *Side view of the sample after structuring and injection molding. White
areas are stainless steel, while the light and dark gray areas are the polymer and
glass fibres of the plastic, respectively. The original surface level before laser
structuring is marked with a dashed red line. The laser generated holes are ap-
proximately 100 $\mu$m deep and 110 $\mu$m in diameter. The fibers are seen to enter the
holes thus contributing to the strength.*

90 mm, the width (x-direction in Fig. 6.2) at the connection point is 9 mm, and the
thickness (z-direction in Fig. 6.2) is 1 mm. An area of 2x5 mm on the tip of the bar
(both sides) is structured with the laser. The structured area is quite small, since
further structuring resulted in a strength of the interconnect leading to breakage in
the plastic, away from the joining region, during the tensile test. After structuring,
the samples are cleansed with acetone and the plastic is injection molded in a ge-
ometry like the steel bar (except for a larger thickness of 4 mm) with an overlap
area between metal and plastic of 1 cm$^2$. Figure 6.2 shows the process from un-
structured steel bar to laser structured steel bar with injection molded plastic part.

Figure 6.3 shows an optical microscope image of the structured and injection
molded interface as seen from the side. The sample is cut through the structured
area and then grinded and polished. The bright white areas represent the remaining
stainless steel, while the light and dark gray are the polymer and glass fibres of the
plastic, respectively. The image shows how the fibres clearly enter the holes and
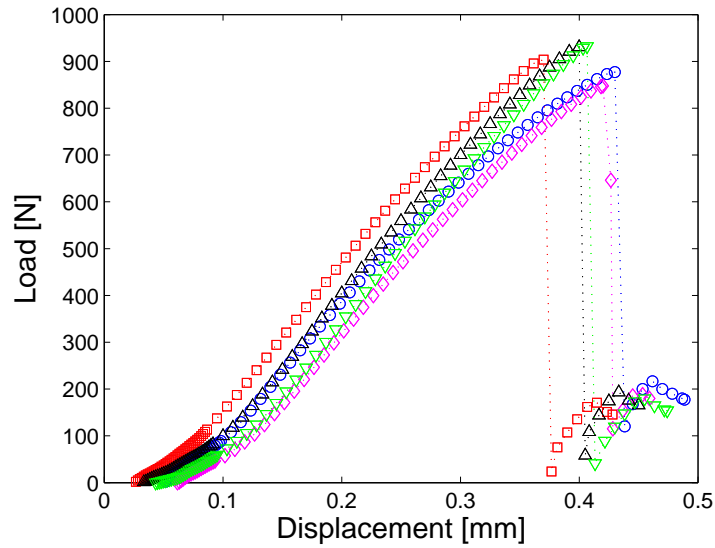
**Figure 6.4.** *Tensile test after structuring and injection molding. The graph shows the fracture test of 5 test bars with identical structuring. The average strength from this set is 898 N with a standard deviation of 16 N.*

thus are expected to contribute to the strength of the interconnect.

A tensile test (ISO 527) yields the ultimate tensile strength (UTS): The joined samples are placed in an Instron 5500R, with each end in a gripper arm and the distance between them is set to increase by 1 mm/min in the $\pm$ y-direction as indicated by the green arrows in Fig. 6.2. The load is simultaneously measured and the UTS of the joint can thus be found. A typical set of tensile tests is shown in Fig. 6.4.

## 6.3   Results and discussion

The strength of the joint will clearly be affected by the distance between holes. As can be seen from Fig. 6.5(a), the strength decreases rapidly with increasing distance between the holes. For comparison it should be noted that the joint strength of the reference samples, identical in every way to the experimental samples except for the laser treatment, is only a few Newton. This means that the adhesion strength has been increased by several orders of magnitude. Since the structured area is always 2x5 mm, a larger distance between the holes corresponds to fewer holes on the samples, and a decrease in strength is therefore expected. To account for this,
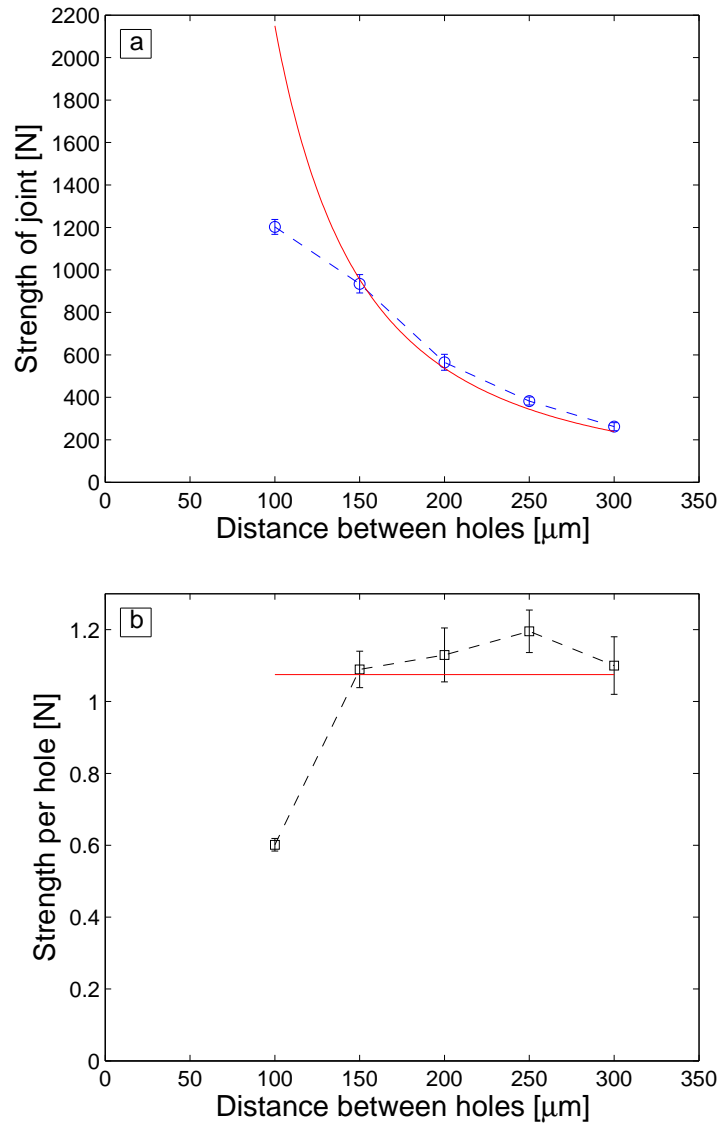
**Figure 6.5.** *(a) Strength of the joint as a function of the distance between the holes. Each point is an average of 15 fracture tests. (b) Strength of the joint divided by the number of laser drilled holes. The depth is 100 μm and the diameter 110 μm. The red lines represent theoretical calculations of the strength, as described in the text.*
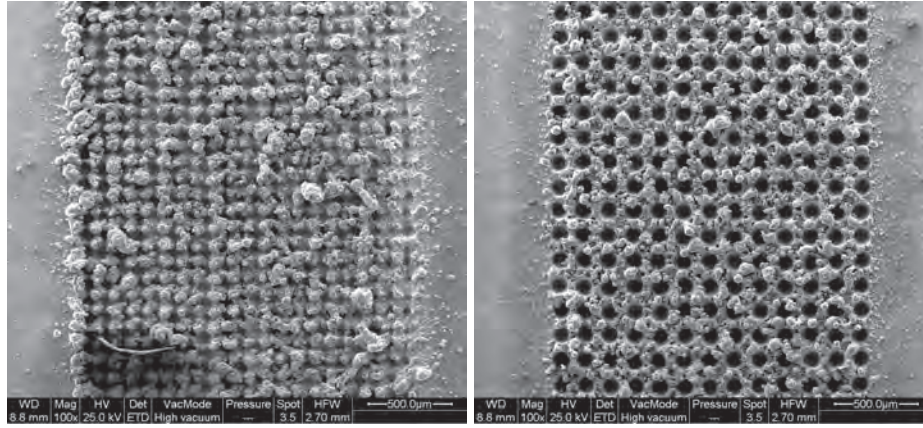
**Figure 6.6.** *SEM images of laser structured surfaces with (a) 100 $\mu$m distance between the holes and (b) 150 $\mu$m distance between the holes.*

the strength in Fig. 6.5(b) has been divided by the number of holes thereby giving a measure of the contribution that each hole makes to the strength.

As can be seen from Fig. 6.5(b), the strength is constant at ~1 N per hole except for the case of 100 $\mu$m between the holes. At this distance there is not enough space to make clearly separated holes, since the holes are approximately 110 $\mu$m in diameter, and the strength per hole is therefore approximately 50 % lower. Scanning electron microscopy images of the laser structured surfaces are shown in Fig. 6.6. The difference between 100 $\mu$m and 150 $\mu$m distance between the holes is clearly seen.

The theoretical strength can be found using the Huber-Mises-Hencky yield criterion [60]. According to this theory the shear strength of the plastic must be $1/\sqrt{3}$ times the tensile strength. Since the plastic in the holes is exposed to shear stress this is the relevant parameter. The tensile stress at break for the plastic is tabulated as 195 MPa [61]. Using an area of adhesion which is simply the total area of the laser-drilled holes, the theoretical UTS of the joint sample can be found as the product of the tensile stress and the area divided by the square root of three. This result is shown by the solid red lines in Fig. 6.5. It is seen that we have excellent agreement except in the case of 100 $\mu$m between the holes, which has already been discussed.

Figure 6.7 shows the measured strength as a function of the hole depth (for a fixed hole spacing of 150 $\mu$m). The strength clearly increases initially but saturates at a value around 1100 N for depths greater than ~100 $\mu$m. Since we structure only 2x5 mm this corresponds to a strength per area of approximately $10^8$ N/m$^2$.
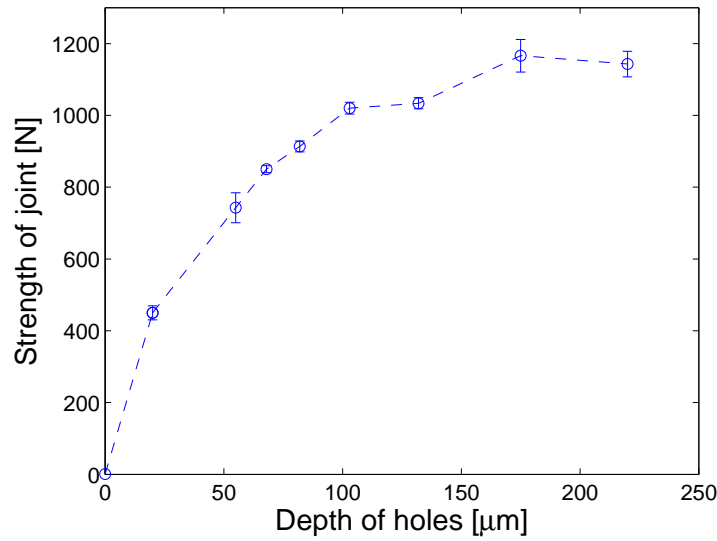
**Figure 6.7.** *Strength of the joint as a function of the depth of the holes. Each point is an average of 15 fracture tests. The spacing between the holes is 150 $\mu$m. The burst mode (e.g. 1x50 pulses) has been applied, see text.*

As will be discussed later, the saturation can be rationalized by the observation that the fracture is typically initiated at a line running along the top of the holes, so beyond a certain depth the increase in the strength becomes negligible.

In some cases a drop in strength was even observed at hole depths of 150 $\mu$m. This is due to the fact that the holes tend to close up after the associated long laser exposure time. This clearly has a detrimental effect on the strength of the interlock. As discussed in chapter 5 this can be circumvented by applying the laser pulses in a sequential way, i.e. returning to each hole a number of times (e.g. 50x1 pulses), instead of applying all the pulses in a burst (e.g. 1x50 pulses). This indicates that local heating of the sample plays a crucial role in the structuring process. In the burst mode the material in and around the hole remains hot for a longer time and the molten material may flow to cover the hole.

To eliminate these effects, the data shown in Fig. 6.7 are taken using the sequential structuring. One must remember, that the production time increases when the array of holes is drilled in the sequential way, since more time is needed to move the laser beam around. Since production time is often an important issue, one may want to apply other means of cooling the sample. The optimization of production time is also discussed in references [4] and [21].
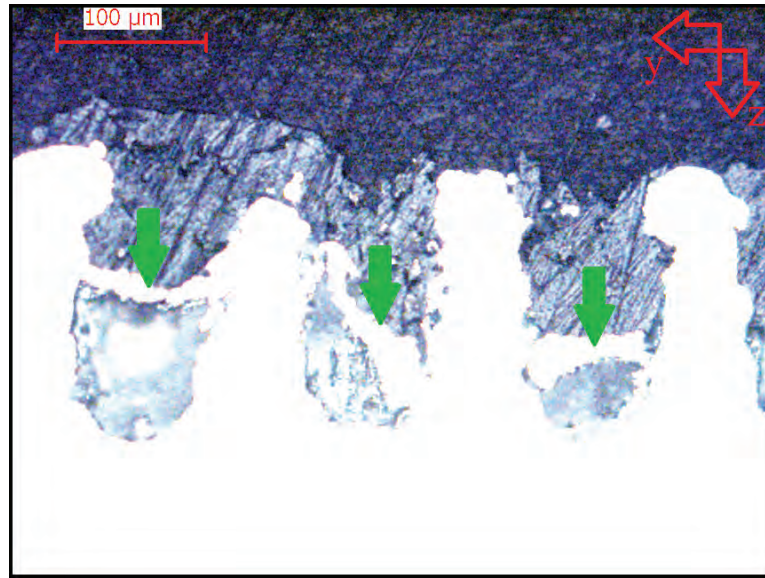
**Figure 6.8.** *Polished sample after structuring and injection molding. White is steel, gray is plastic and black is epoxy used for fixating the sample during polishing. It is seen that the plastic has filled the holes and that the fracture happens as a locus of failure running along the top of the holes. Also, one can see that in some cases, the recast material is pushed into the hole (marked with green arrows), presumably during the injection molding process.*

A side view of a test bar after structuring, injection molding, and fracture test is shown in Fig. 6.8. As before, the white area is steel and the gray area is plastic, while the black in this case is epoxy (used for fixating the sample during polishing). Again it is seen that the plastic is injected into the holes. However in some cases the recast material is pushed into the holes thereby preventing the plastic from reaching the bottom (indicated by green arrows in Fig. 6.8). Other effects that may prevent plastic from being fully injected are pressure build-up and surface tension.

Also it can be seen why the strength saturates at large hole depths: The fracture is always initiated along a line joining the top of the holes, so a continued increase in depth will not contribute to the strength. There are several possible fracture mechanisms for fiber-reinforced polymers [62]. Fracture is, however, typically controlled by numerous micro-cracks distributed throughout the material. In the present situation, it is highly likely that fracture will be initiated near the adhesion interface due to the notch effects introduced by the surface roughness.

For many industrial applications the samples must be resistant to temperature
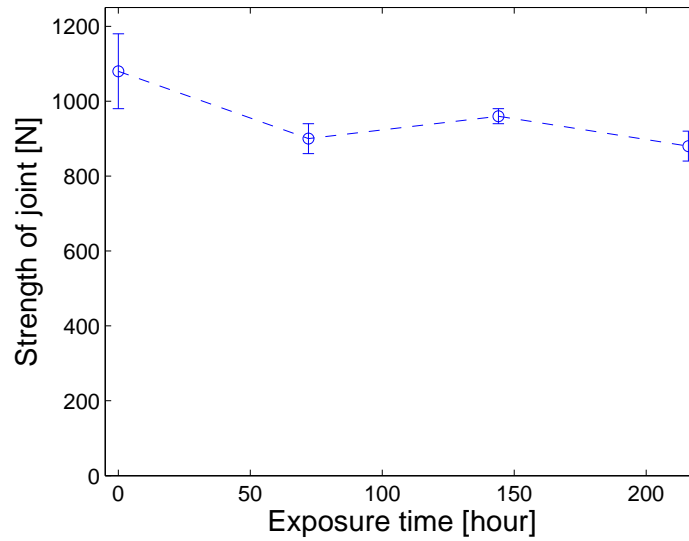
**Figure 6.9.** *Temperature fluctuation test. The joint sample exhibits very good resistance to temperature fluctuations.*

fluctuations. To examine this, the structured and injection molded test bars are placed in a climatic test cabinet, which goes from -60 °C to 160 °C every 2 hours. As can be seen from Fig. 6.9, the strength is roughly independent of the duration that the samples are exposed to the temperature fluctuations.

## 6.4   Conclusion

We have demonstrated a way to increase the adhesion strength between metal and plastic by several orders of magnitude using laser structuring of the metal surface followed by injection molding of the plastic into the surface. The optimum parameters for material removal with a Nd:YLF laser were found in chapter 5, while this chapter determined the strength of the adhesion at different hole densities and hole depths. The obtained strength per area is of the order $10^8$ N/m$^2$. Theoretical calculations of the strength are in excellent agreement with the experimental data. Furthermore, the mechanism for joint failure has been determined by investigating the fracture point: The break is initiated in the plastic along a line joining the top of the holes. Finally the resistance to temperature fluctuations have been examined and appears to be excellent.

# CHAPTER 7

# MMI continued: Optimizing the normal strength of micro-mechanically interlocked joints

The shear strength of micro-mechanically interlocked joints was investigated in chapter 6. In this chapter the normal strength shall be examined. For MMI to be a flexible technique, applicable for numerous applications, it must have a high strength in both these directions. We show that the strength per hole in the normal direction is approximately a factor of 10 smaller than the shear strength and that adhesion strength per area is of the order of $10^7$ N/m$^2$.
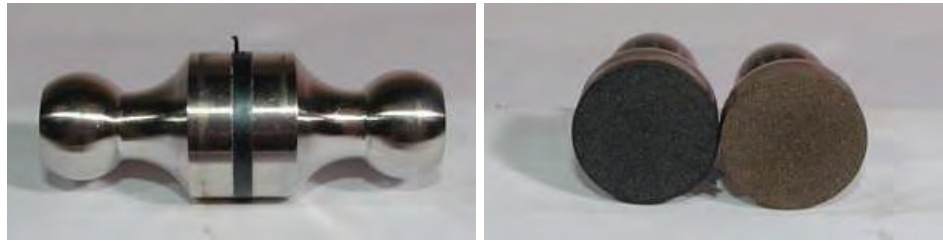
**Figure 7.1.** *The test piece used for finding the normal strength of micro-mechanically interlocked samples. The two metal pieces are laser structured and plastic is injection molded into the gap between them. The test sample seen before (left) and after (right) the fracture test.*



**Figure 7.2.** *Setup for measuring the ultimate tensile strength (in the normal direction, i.e. out of the holes) of the micro mechanically interlocked samples.*

## 7.1   Materials and methods

The laser parameters and materials applied were described in section 6.2. However, the test samples are naturally different from those used to test the shear strength. The metal piece is shaped like a ludo piece as shown in Fig. 7.1

The large end, having a diameter of 20 mm, is laser structured and two pieces are joined together by injection molding plastic into the gap. The structured area is 314 mm$^2$, i.e. more than 30 times larger than the structured area for the shear strength. As in chapter 6 a tensile test according to ISO 527 yields the ultimate tensile strength (UTS). The setup for measuring the UTS is displayed in Fig. 7.2. The distance between the gripper arms is set to increase by 1 mm/min while the load is measured. For all the experiments 5 samples were made with identical laser structuring and the mean value with corresponding standard deviation are shown.

## 7.2   Results and discussion

The strength of the joint as a function of the distance between the holes is shown in Fig. 7.3. Strengths in the kN regime is observed which corresponds to approximately $10^7$ N/m$^2$. This is around a factor of 10 lower than the observed shear strength. This is also expected since the normal force pulls the plastic out of the holes in contrast to the shear force which is perpendicular to the holes. Again it should be noted that when no laser structuring is applied the samples simply fall apart so the interlocking strength has been increased by several orders of magnitude.

Since a constant area of 314 mm$^2$ is always structured, a larger distance between the holes implies fewer holes on the sample, so a decrease in strength is expected. To compensate for this the strength in Fig. 7.3(b) has been divided by the number of laser drilled holes. A constant value of $\sim$ 0.1 N per hole is observed. This of course again corresponds to an order of magnitude lower strength than what was found for the shear strength.

It is seen from Fig. 7.3(a) that the strength has an $x^{-2}$ dependence on the distance between the holes. Since the number of holes on the sample scales as $x^2$ this corresponds to a constant strength per holes as observed in Fig. 7.3(b). However, a theoretical strength cannot be computed as in section 6.2 due to the diverse fracture mechanics in the normal direction as will be discussed later.

Unlike the case in Fig. 6.5(b) no reduction in strength is seen at 100 $\mu$m distance between the holes. This indicates that the normal strength of the joint is less dependent on the specific surface geometry compared to the shear strength. This can partly be explained by the fact that in the case of normal strength the force is exerted out of the holes and the joint strength is therefore not directly related to the holes but more to the general roughness in the direction parallel to the surface. If the scenario was as simple as displayed in Fig. 6.1 the normal strength would be much lower than what is observed.

A polished sample after structuring and injection molding is seen from the side in Fig. 7.4 where the white part is steel and the gray part is plastic. Note the random roughness in the direction parallel to the holes. Also it should be noted that the plastic does not entirely enter the hole and thereby does not fully contribute to the strength.

Turning to the strength of the joint as a function of the depth of the holes it becomes somewhat more complicated. Since the normal strength originates from the roughness and not directly from the holes themselves the strength will be highly dependent on the specific surface geometry of the individual sample.
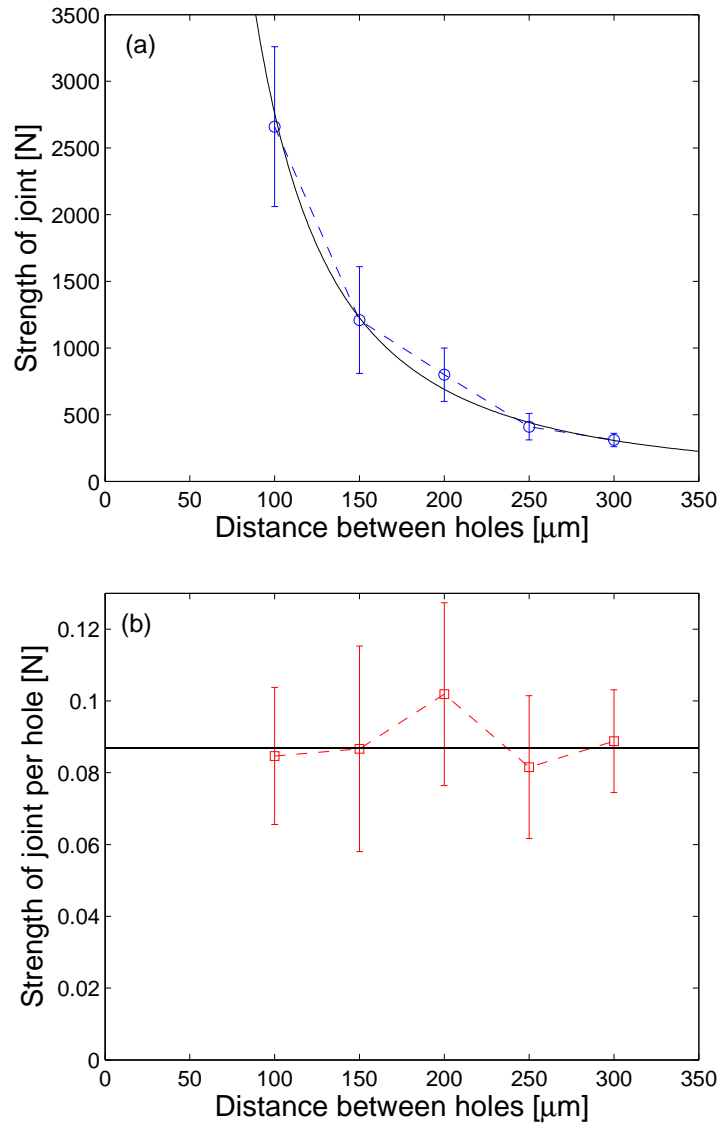
**Figure 7.3.** *(a) Strength of the joint as a function of the distance between the holes. The black lines represents a least square fit to $a \cdot x^{-2}$. (b) Strength of the joint divided by the number of laser drilled holes. The black lines represents a least square fit to a constant value. A constant depth and diameter of 100 $\mu$m and 110 $\mu$m is applied.*

Figure 7.5 shows the strength of the joint as a function of the depth of the holes for constant diameter and distance between the holes (i.e. the same number of holes
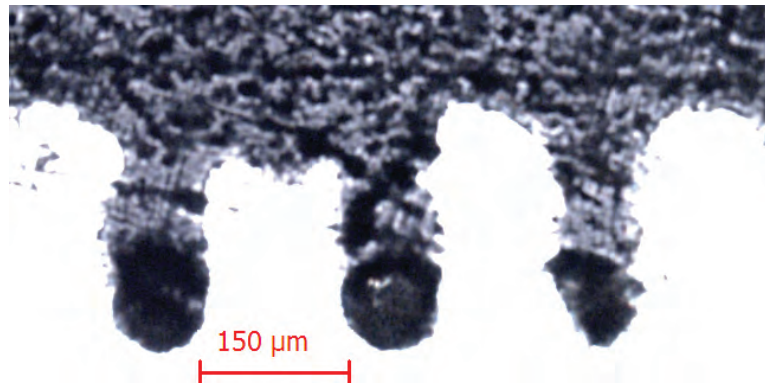
**Figure 7.4.** *Sample seen from the side after laser structuring and injection molding. White is steel (in which the laser has drilled holes) and gray is plastic.*



**Figure 7.5.** *Strength of the joint as a function of the depth of the holes for samples structured with 1x?? pulses. The diameter of the holes is 110 $\mu$m while the distance between the holes is 150 $\mu$m.*

on each sample). The blue circles, red squares and black triangles represent three different series with identical structuring. Each point corresponds to an average of 5 fracture tests and the error bars are given by the $1\sigma$ standard deviation. In Fig. 7.5 the samples are structured in the burst mode, i.e. 1x?? pulses (for instance 1x56 pulses yields a hole depth of 100 $\mu$m).
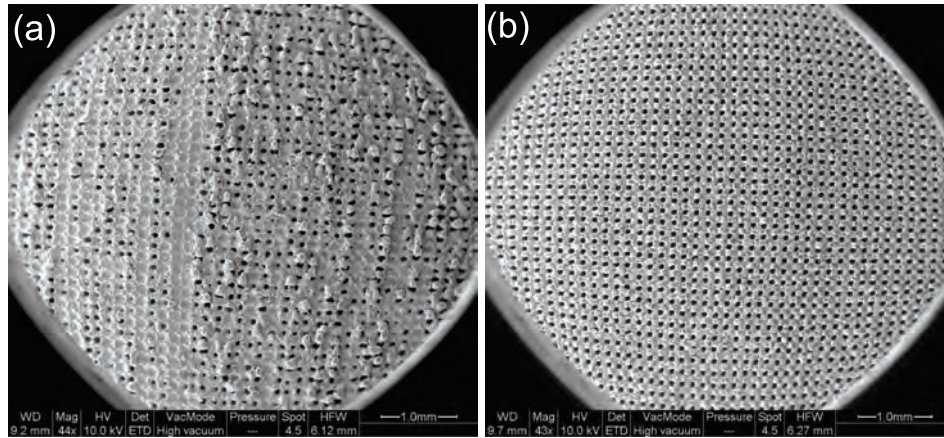
**Figure 7.6.** *(a) Large areas of closed holes are observed when the burst mode is applied (in this case 1x86 pulses). (b) Applying the pulses in a sequential mode (in this case 5x23 pulses) prevents the holes from closing up.*

Again strengths in kN regime are seen. However large variations between the different series are observed. We stress that the exact same procedure has been applied with constant parameters throughout the three series, so there is no reason to expect different results. Particularly in the range from 100 $\mu$m to 150 $\mu$m the variations are pronounced. As discussed in the previous chapters, the holes tend to close up during nanosecond laser structuring. Especially when large areas ($>100$mm$^2$) are structured, the associated long exposure time (many seconds and in some cases minutes) heat the sample to a level where liquid material flows to cover the holes.

The individual samples have been investigated in a scanning electron microscope (SEM) both before and after fracture test, but no connection between the detailed surface topography and the strength was observed. Also, a high speed camera (1000 fps) was used to record the fracture test in order to identify the fracture process, but no differences were observed. All that could be observed with the high speed camera was that the fracture was initiated at the edge of the sample. This leads us to conclude that fracture is initiated at a weak-point along the edge of the sample.

Figure 7.6 shows SEM images of laser structured samples. The sample shown in 7.6(a) is structured using the burst mode, whereas the sample shown in 7.6(b) is structured using the sequential mode, in this case 5x23 pulses, i.e. 23 pulses in each holes repeated 5 times for the array of holes.

It is seen that in the sequential mode the material have had time to cool before repeated irradiation and molten material has therefore not covered the holes. Figure

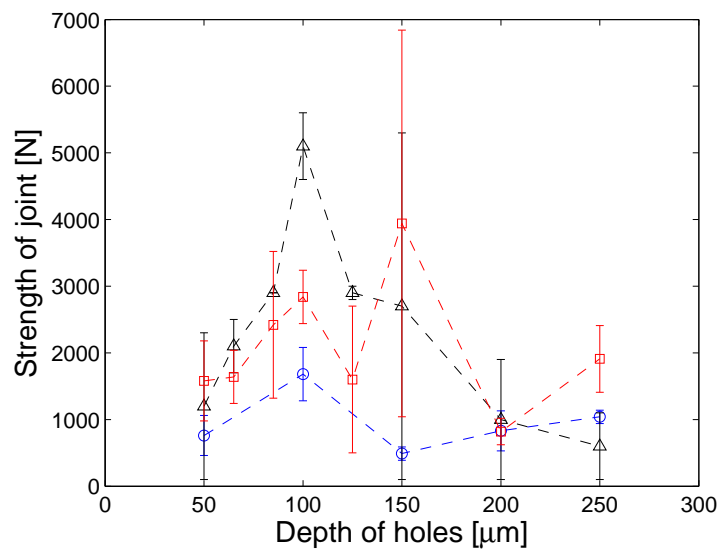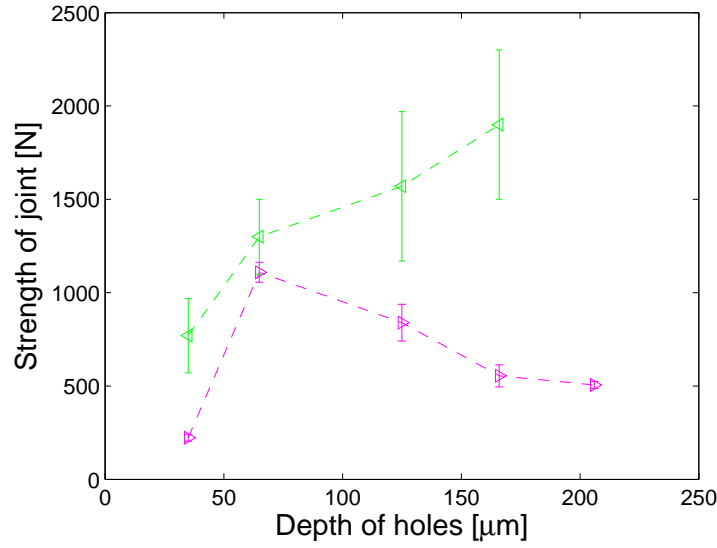**Figure 7.7.** *Strength of the joint as a function of the depth of the holes for samples structured with 5x?? pulses. The diameter of the holes is 110 $\mu$m while the distance between the holes is 150 $\mu$m.*

7.7 shows the joint strength as a function of the depth of the holes structured in the sequential mode. As before the green left-pointing triangles and the purple right-pointing triangles represent different series with identical structuring. Each point corresponds to an average of 5 fracture tests and the error bars represent the $1\sigma$ standard deviation.

Even though the surface topography is much more regular and no closed holes are observed there are still large variations between the series. Experiments where the structuring was performed in an argon atmosphere were also conducted, but no systematic improvement was found. Inspection of the samples after fracture test shows that the plastic is pulled out of the holes leaving one of the ludo pieces with all the plastic and the other one without any plastic, see Fig. 7.1. It is thereby not a fracture as described in section 6.3 where we observe fracture in the plastic along a line joining the top of the holes. In the case of normal strength it is more a joint failure due to the fact that the plastic is pulled out of the holes.

## 7.3 Conclusion

We have measured the normal strength of micro-mechanically interlocked joints. A strength of $\sim 0.1$ Newton per laser structured hole was observed and strengths of the order $10^7$ N/m$^2$ was achieved. This is about a factor of 10 lower than the shear strength of MMI samples as discussed in chapter 6. The strength of unstructured samples are only a few Newton so we have increased the adhesion strength by several orders of magnitude when structuring samples with an area of 314 mm$^2$.

The normal strength was shown to have an $x^{-2}$ dependence on the distance between the holes, corresponding to a constant contribution to the strength from each laser drilled hole. The depth of the holes was shown to have a more complicated effect on the joint strength. Interlocking in the kN regime was found but the observed strength of the joint could not be precisely predicted. Most likely this is due to a somewhat random fracture mechanism, where the fracture is initiated at a weak-point at the edge of the sample and the plastic is being pulled out of the holes.

# CHAPTER 8

## Testing the permeability and corrosion resistance of micro-mechanically interlocked joints.

As shown in the previous chapters, micro-mechanical interlocking can provide adhesion between metal and plastic of very high strength. However, the water permeability and corrosion resistance of the joints must be examined. For many industrially relevant applications it is important to keep water away from certain parts and to prevent the sample from corroding. A thorough study of the permeability of the interconnected samples at different temperatures and after employing different laser-structuring techniques is conducted. The permeability seems to be consistent with the Hagen-Poiseuille equation independent of the laser structuring technique and is orders of magnitudes larger than the diffusion rate through the plastic. Two different types of corrosion tests have been undertaken, and we show that care must be taken in order not to degrade the corrosion resistance of the sample to an unacceptable level.

This chapter is based on the article "Testing the permeability and corrosion resistance of micro-mechanically interlocked joints", submitted to Journal of Colloid and Interface Science.

## 8.1   Introduction

Although very high joint strengths can be obtained the interconnect may still contain small channels or pores that can lead to undesired water permeability. In some industrial applications the environmental protection of sensitive electronic equipment will rely on the sealing between metal and polymer, and it is therefore of utmost importance to prevent the interconnect from leaking more than acceptable.

Stainless steel continues to be a widely used material due to its good mechanical properties and corrosion resistance. However, laser structuring is a somewhat aggressive treatment, which may cause a reduction in the corrosion resistance. While it is difficult to avoid some extent of surface oxidation during the laser ablation, the effect can be significantly reduced if the structuring is performed under an inert argon atmosphere.

In the present chapter the mechanisms behind both the permeability and the corrosion degradation of the interconnect are examined. For the MMI technique to be applicable in e.g. pump manufacturing and protection of electronics, these mechanisms must be fully understood and modeled for life-time predictions.

## 8.2   Experiment

From the previous chapters we know that the surface topography is highly dependent on the laser irradiation strategy. When constructing a matrix of e.g. 100x100 holes, the diameter, depth and shape of the holes change when applying the laser pulses in a burst of e.g. 1x50 pulses compared to the sequential strategy of returning to each hole a number of times e.g. 5x10 pulses. In the corrosion tests, both these irradiation strategies have therefore been employed.

In the permeability tests different irradiation strategies have also been applied. Three types of laser written structures have been made: "Holes", "Lines" and "Lines+Holes". The specific details will be clarified in section 8.3.1.

To test the permeability of the joints, a sample as shown in Fig. 8.1 is constructed. First the inner side of the metal ring is laser structured (checkered area in Fig. 8.1(c)). The plastic is then injection molded onto the structured side of the metal providing a cylindrical cup. This composite item is placed inside a larger metal cup with a small hole in the bottom. The two parts are welded together and 10 ml of water is filled into the sample. Finally the small bottom hole is closed in a short spot welding process.

The samples are then placed in ovens at temperatures of 40, 70, 110 and 150 degrees Celsius. This corresponds to a pressure inside the sample of 1.07, 1.31,
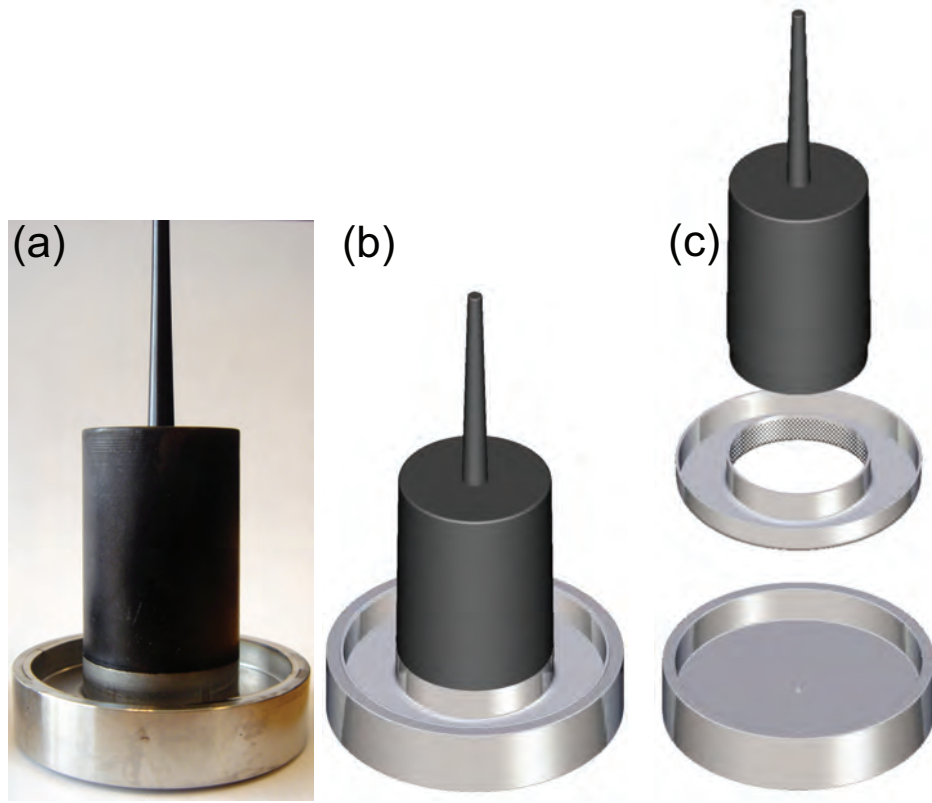
**Figure 8.1.** *(a) Photograph of a sample used for testing the permeability of the MMI joint. The bright part is stainless steel and the black part is plastic (b) CAD drawing of the sample. (c) Exploded view of the sample. The checkered region, on the inner side of the metal ring, represents the laser structured area. The metal ring has a height of 8 mm and an inner diameter of 27 mm*

2.43 and 5.76 bars respectively [63]. The permeability is found by weighing the samples at fixed time intervals.

## 8.3    Results and discussion

### 8.3.1    Testing the permeability of MMI joints

The permeability as a function of the oven temperature is shown in Fig. 8.2. As can be seen the permeability changes dramatically over the applied temperature interval. The blue circles, red squares and green triangles represent different laser written structures as discussed below.

Water transport across an interface or through a polymeric membrane can be divided into hydraulic and diffusive transport. When porous materials are considered the fluid can enter the material either as a liquid or as a gas and the pressure gradient over the material will drive the movement of the fluid through the pores. The flow rate will depend on factors such as the geometry, viscosity and the capillary action. Typically the dimensions of the pores by far exceed the size of individual molecules and transport is thus collective, i.e. includes solutes, etc. The relationship describing this method of transport is referred to as the Hagen-Poiseuille equation and describes the pressure drop in an incompressible fluid flowing through a long cylindrical pipe (pore).

$$Q = \frac{1}{8\eta L}\Delta p r^4.$$ (8.1)

In this context, $Q$ is the volumetric flow rate, $\Delta p$ is the pressure drop over the pore, $r$ is the radius of the pore, $\eta$ is the dynamic viscosity of the fluid and $L$ the length of the pore. Laminar flow and a constant circular cross-section have been assumed.

If the length of the structured area (the shortest geometrical path is estimated to be 8 mm) is considered along with tabulated numbers for the viscosity of water, at the different temperatures applied, we find that a pore diameter of approximately 1.8 $\mu$m reproduces the experimental findings quite nicely, see the black solid line in Fig. 8.2.

Three different laser structuring techniques have been applied. In all cases the metal sample is mounted on a continuous rotation stage, which is tilted approximately 110° compared to the laser beam direction (note that 90° would correspond to normal incidence). The technique labeled "Holes" corresponds to the metal being structured with an array of holes having a pitch of 150 $\mu$m in the horizontal direction and 200 $\mu$m in the vertical direction as shown in Fig. 8.3(a). The holes are $\sim$ 100 $\mu$m deep. In the technique labeled "Lines" the sample is rotated a number of rounds while the laser beam is rapidly swept across the surface. Hereby grooves with a pitch of 200 $\mu$m and a depth of $\sim$ 100 $\mu$m are formed, see Fig. 8.3(b). Finally the "Lines+Holes" samples are structured with alternating holes and lines with a pitch between the features of 200 $\mu$m in the horizontal direction and 300 $\mu$m between the holes in the vertical direction, see Fig. 8.3(c).

As can be seen from Fig. 8.2 the three different techniques give rise to very similar permeability and the "Holes" technique would therefore be preferable since it is by far the fastest way of structuring the samples.

It should be noted that the calculated mass transport can also be accomplished
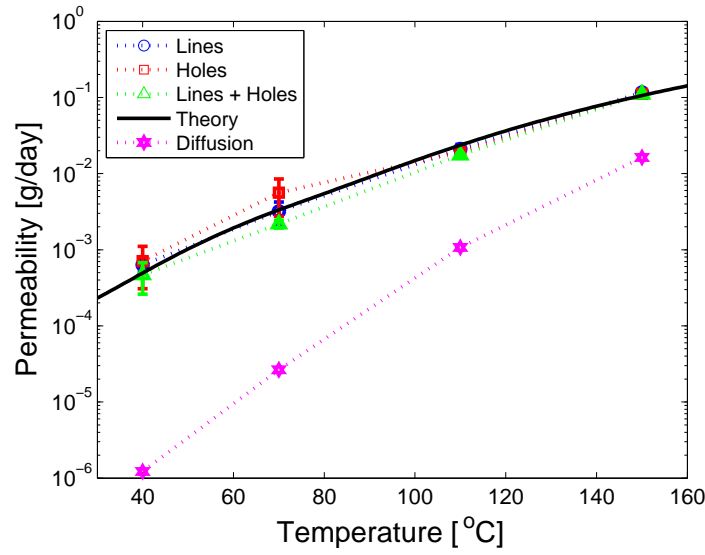
**Figure 8.2.** *Permeability versus temperature for different structuring techniques. The black curve is a plot of Eq. (8.1) with a pore radius of r=1.8 μm. The blue circles, red squares and green triangles represent different laser structuring techniques while the purple stars represent the diffusion rate through the plastic, as described in the text.*

by a number of other geometries. In fact, 5 pores with a radius of 1.2 $\mu$m along an 8 mm cylinder leads to the same net mass transport as a single pore of radius 1.8 $\mu$m. Also, a single pore of 2 $\mu$m radius along a 12 mm cylindrical path would reproduce the observed permeability. In addition, when "lines" were included in the structuring, the mass transport is expected to take place over a longer distance than the aforementioned 8 mm. The structuring of the surface may therefore significantly increase the permeation path length and thus a larger diameter of the pore is possible. However, the experiments seemingly indicate that the permeation length plays little or no role for the overall mass transport. While our experiment cannot distinguish between these scenarios, we do, however, often observe limestone at one or more locations along the plastic-metal interconnect, indicating that collective transport through a few pores is the dominating process.

While our data could be reasonably reproduced by Eq. (8.1) it is also important to account for the intrinsic diffusion of water through the polymeric side wall.

The mechanism of water transport through compact materials is expected to be diffusion of individual molecules where the fluid is absorbed in assumed defect-
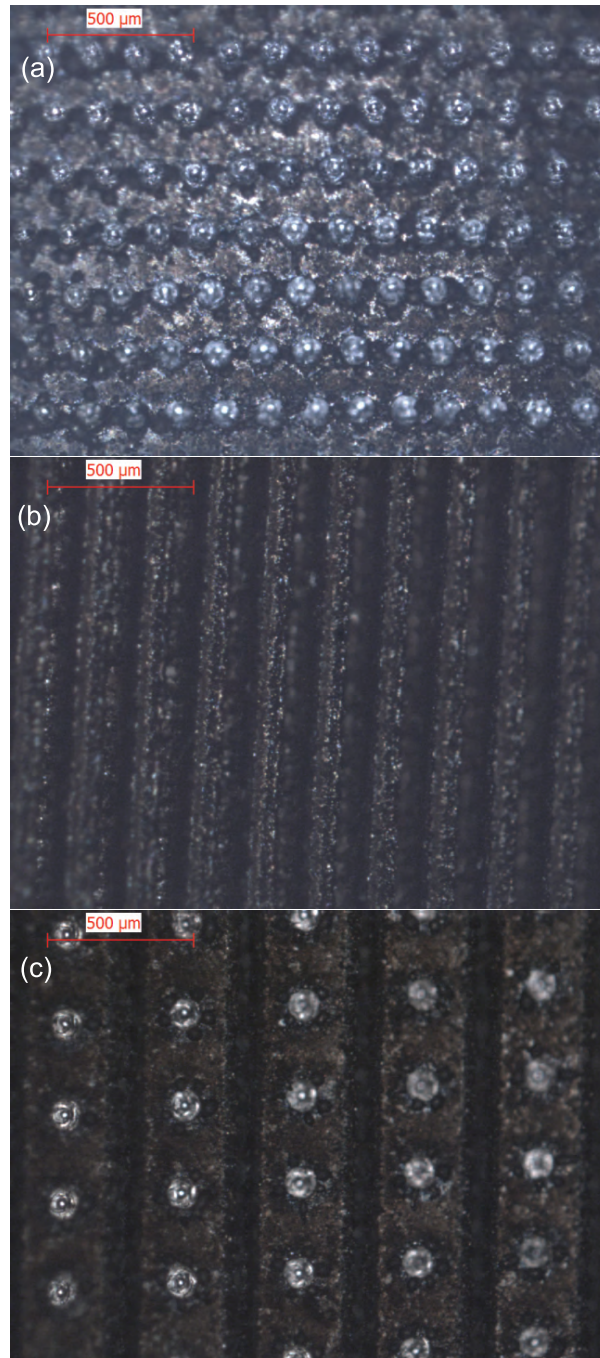
**Figure 8.3.** *Optical microscope images of samples structured with the different techniques: (a): "Holes", (b): "Lines", (c): "Lines+Holes". The details are described in the text.*

free materials. Absorbed molecules then move as individual particles by a random walk which in combination with a concentration gradient results in a net diffusion flux. Transport is influenced by the material thickness, contact area, and chemical affinity between water and hosts, as well as temperature. The pressure difference plays little or no role.

Since the molecules are transported individually, solutes are retained on the upstream side of the material. Experimentally, a sheet with dimensions that by far exceed the thickness of the material is immersed in water at the required temperature and the mass followed over time. Once steady state has been achieved, equilibrium water uptake, diffusion coefficient, and thus permeability of the material can be extracted using well described mathematical relationships [64]. The permeability values can then be used to estimate the steady state water transport across the polymeric membrane of our items.

We have determined the permeability of PPS at temperatures of 75°C, 95°C, and 110°C and used these values to predict the behavior at 40°C, 70°C and 150°C by a conventional Arrhenius relationship. Since the equilibrium water uptakes at 40°C, 70°C, and 150°C are not known, the values measured at 75°C and 110°C, respectively, are used to represent the values at 40°C and 70°C (75°C) and 150°C (110°C). The actual permeability at 150°C is expected to be marginally higher as the equilibrium water uptake increases marginally with temperature.

It should be emphasized that the estimates represent the expected steady-state value and does not, *per se*, take the initial permeation build up into account. They can therefore be understood as upper limits. Nonetheless, these values are significantly lower than the experimentally measured permeability rates as seen in Fig. 8.2, and it is reasonable to assume that diffusive transport plays only a marginal role.

### 8.3.2   Testing the corrosion resistance of MMI joints

Since nanosecond laser structuring in air provides an opportunity for the surface to oxidize, care must be taken not to degrade the corrosion resistance of the material. Two different types of tests have been performed: A salt spray test according to the EN ISO 4628 standard and an $FeCl_3$ test according to ASTM G48 standard. The test samples are round stainless steel type DIN 1.4301 plates with a diameter of 42 mm. Two different quantities of laser-structuring are applied: (i) a square in the center of the sample with an area of 1 $cm^2$, as seen in Fig. 8.4 and (ii) structuring of the entire area of one side of the sample.

In the salt spray test, the samples are exposed to an artificial salt spray atmo-
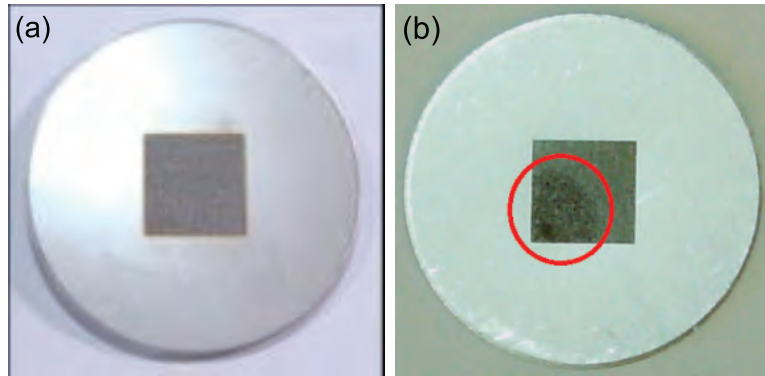
**Figure 8.4.** *Samples for testing the corrosion resistance. The central 1 cm$^2$ has been laser structured. (a) shows the sample after laser structuring but before the corrosion test while (b) shows the sample after a salt spray test, as described in the text. The red circle indicates the corrosion damaged area.*

sphere with a concentration of 5% NaCl at a temperature of 35°C. Possible results of this test are Ri0 (0% covered by corrosion), Ri1 (0.05% covered by corrosion), Ri2 (0.5% covered by corrosion), Ri3 (1% covered by corrosion), Ri4 (8% covered by corrosion) and Ri5 (40-50% covered by corrosion). The results of the salt spray test are shown by the green data points in Fig. 8.5.

In the corroded parts, the corrosion occurs essentially in the structured area as indicated by the red circle in Fig. 8.4(b). For the unstructured samples, 0% corrosion is observed in the test. It should be noted, that when 1 cm$^2$ is laser structured, the samples processed in ambient atmospheric air exhibit a larger degree of rusting compared to samples processed in an inert argon atmosphere. Finally, we see that if the entire area of one side of the sample is structured the result is Ri5, i.e. more than 40% of the sample surface shows sign of corrosion. Since Ri5 is the highest category in this test, the result could in principle be much higher than 40%.

In the FeCl$_3$ test, the parts are exposed to a FeCl$_3$ solution in a concentration of 0.75% FeCl$_3$ at a controlled temperature of 20°C for a period of 24 hours. The corrosion damage is quantified as the weight loss of the sample during the test divided by the total surface area.

Structuring 1 cm$^2$ in ambient atmospheric air is seen to increase the weight loss compared to the unstructured samples by roughly 50%. When structuring is undertaken in an argon atmosphere an increase of only $\sim$ 10% is observed. It should be noted, that according to the ASTM G48 standard, a total weight loss of 1 g/m$^2$, is considered acceptable. So depending on the application the degradation in corrosion resistance may be tolerable.
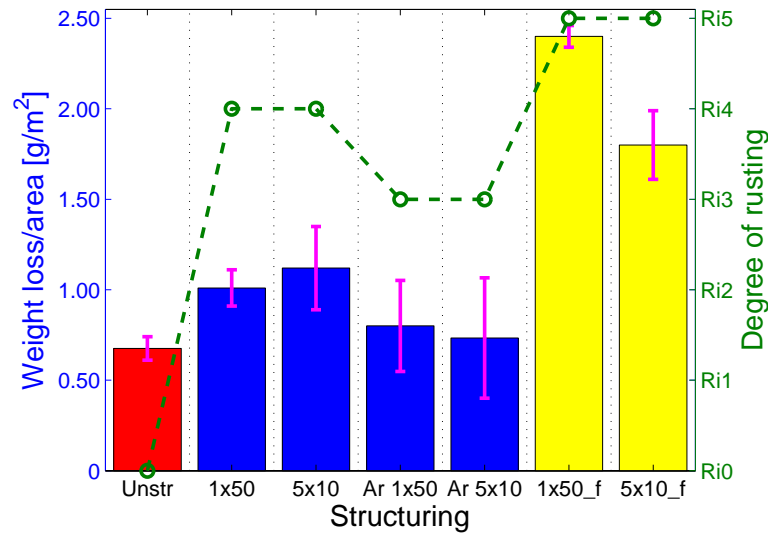
**Figure 8.5.** *The results of the corrosion tests for different laser structuring techniques. The bars represent the weight loss during the FeCl$_3$ test divided by the total sample area and are related to the left y-axis. The green circles connected with a dashed line represent the results of the salt spray test and are related to the right y-axis. Red represents unstructured samples, blue represents samples where 1 cm$^2$ has been structured and yellow represents samples where the entire area of one side ($\sim$ 14 cm$^2$) has been structured. Each data point is an average over 3-5 measurements and the purple error bars indicate the 1$\sigma$ standard deviation.*

However, for the samples where the entire area of one side of the sample is laser structured, the weight loss is roughly a factor of 3 higher than for the unstructured samples and thus not inside the acceptable region. The results indicate that the sequential laser structuring technique (i.e. 5x10 pulses) results in a smaller weight loss compared to the technique where all the pulses are applied in one burst (i.e. 1x50 pulses). The reason this phenomenon is not observed for 1 cm$^2$ structuring is that the laser irradiation strategy becomes increasingly important as larger areas are structured.

The weight loss per structured area could also be considered. For the samples with 1 cm$^2$ structuring processed in atmospheric air this would correspond to approximately 30 g/m$^2$. However, this seems to be inconsistent with the fully structured samples, which gives a weight loss per structured area of approximately 4 g/m$^2$. This indicates that a scaling according to the structured area is not valid.

## 8.4  Conclusion

We have studied the permeability of micro-mechanically interlocked samples. It was shown that diffusion through the polymer part is several orders of magnitude lower than the observed permeability, which indicate that collective transport is dominating. The permeability of the interconnect at different temperatures and after employing different laser structuring techniques was investigated and shown to be consistent with the Hagen-Poiseuille equation. Surprisingly it was independent of the laser structuring technique and the experiments indicated that a few micrometer-sized channels were responsible for the transport of water through the interconnect.

Two different types of corrosion tests were undertaken. We showed that the corrosion resistance of the samples were reduced, but depending on the application and the amount of material undergoing laser structuring the degradation could be within the acceptable range. It was shown that when laser structuring was performed in an inert argon atmosphere the reduction in corrosion resistance was somewhat lower than for samples structured in ambient atmospheric air.

# CHAPTER 9

# Summary

In the present thesis, short-pulse laser ablation of metals is studied. In the first part of the thesis, a combination of experimental work and computer simulations is presented in order to identify the fundamental mechanisms behind the ablation process. In the second part, short-pulse laser surface structuring is applied to create very strong adhesion between metal and plastic in a process called micromechanical interlocking.

Experimental femtosecond laser ablation studies of the metals copper, silver and tungsten are presented. Threshold fluence and incubation coefficients are found by varying the laser fluence and the applied number of pulses. The ablation rates in the regimes of high and low fluence is examined. In the low-fluence regime, a logarithmic dependence is found, while the high-fluence data are consistent with a linear dependence. Both dependencies can be explained by approximate analytical equations originating from the two-temperature model.

Computer simulations of the two-temperature model are performed. The simulations provide interesting insight into the fundamental aspects of the ablation process. By varying the laser pulse duration, the threshold fluence and melting depth (heat affected zone) are found to be constant for pulses shorter than 1 picosecond while they increase as $\sqrt{\tau}$ for pulses longer than $\sim 40$ picoseconds. By comparing with the experimental data it is found that ballistic electrons must be incorporated into the model to explain the observed penetration depths for the noble

metals, while this effect is negligible for tungsten.

An experimental setup capable of measuring the reflectance and ablation rate of samples undergoing femtosecond laser ablation is presented. The experimental data are compared to a model relating the reduction in reflectance to the evolution of ripples forming in the area of the laser spot. The model is shown to be consistent with the data and provides information about the varying reflectance, scattering and absorptance of the sample undergoing structuring.

In the more applied part of the thesis, a nanosecond laser system is performing the surface structuring. It is examined how the ablated surface structures depend on the applied laser parameters and the pulse irradiation strategy. It is shown that the generated topography is highly dependent on the temperature. If the material is allowed to cool off, the holes will be smaller and the recast is building up burr locally around the holes. Theoretical calculations of the temperature dependent reflectance is shown to be consistent with the observed decrease in hole size.

Exceptional adhesion between stainless steel and plastic is demonstrated. The metal sample is laser processed and a high quality interconnect is ensured by directly injection molding plastic into the laser-structured surface. The dependence of the mechanical strength of the joint on the exact laser generated surface morphology is investigated. It is shown that appropriate surface structuring can increase the bonding strength by several orders of magnitude, yielding interlocking of very high mechanical stability.

Finally the permeability and corrosion resistance of the micro-mechanically interlocked joints are investigated. The permeability seems to be consistent with the Hagen-Poiseuille equation independent of the laser structuring technique and is orders of magnitudes larger than the diffusion rate through the plastic. It is shown that care must be taken in order not to degrade the corrosion resistance of the sample to an unacceptable level.

# CHAPTER 10

# Dansk Resumé

Laseren blev første gang demonstreret i 1960 [1]. Meget er sket siden, og i dag finder man lasere næsten overalt. Alle kender laser-pointeren og stregkodelæseren fra supermarkedet, men utallige anvendelser finder sted indenfor områder som bl.a. telekommunikation, bil-industri, forskning, rumfart og underholdning.

Man skelner imellem kontinuerte og pulserede lasere. Denne afhandling omhandler den pulserede type. Her får man energien fra laseren ud i små veldefinere pakker (pulser), og man har derfor stor frihed til at deponere energien på en overflade, præcis som man har brug for. Da man kan styre hvor meget energi der skal være i hver puls, hvor hurtigt de skal komme efter hinanden, hvor stort et område af en overflade de skal belyse samt mange andre parametre, er den pulserede laser et utroligt fleksibelt værktøj.

I denne afhandlig beskrives anvendelser af to forskellige typer pulserede lasere. I den mere grundvidenskabelige del af afhandlingen (kapitel 2 til 4) er en femtosekund laser benyttet. Altså en laser med en pulslængde på nogle femtosekunder (1 femtosekund = 0.000000000000001 sekund). Så kort et tidsrum er svært at forholde sig til. På 100 femtosekunder, som er en typisk længde af de anvendte pulser, vil lyset kun nå at bevæge sig 30 mikrometer (0.03 millimeter) - altså cirka tykkelsen af et hår. Tidsmæssigt kan man sige at 1 femtosekund forholder sig til 1 sekund som 7 minutter forholder sig til hele universets alder (cirka 14 milliarder år).

I anden del af afhandlingen (kapitel 5 til 8), som har fokus på anvendelser af laseren, benyttes en laser med en pulslængde på nogle nanosekunder (1 nanosekund = 0.000000001 sekund). Denne type laser har typisk været mere industrivenlig end femtosekundlaseren, da den bl.a. har en større middeleffekt - altså i gennemsnit leverer en større mængde energi pr. tid end femtosekundlaseren.

I denne afhandling beskrives hvordan energien i laserlyset benyttes til at fjerne materiale fra metaloverflader. Dette kan gøres meget kontrolleret og små præcise strukturer i overfladen kan dermed laves. I den grundvidenskabelige del af afhandlingen studeres primært hvordan materialet reagerer, når det absorberer de ultrakorte laserpulser. En fundamental forståelse af hvad der sker, specielt når mange pulser kommer efter hinanden, er nødvendig for at femtosekundlasere for alvor kan blive anvendelige i industrielle sammenhænge.

De strukturer man danner på metaloverfladerne kan bruges til et væld af forskellige ting. Blandt andet kan materialets optiske, tribologiske, biokompatible og vedhæftningsmæssige egenskaber kontrolleres. I den anvendte del af denne afhandling studeres hvordan de lasergenererede strukturer kan benyttes til at lave en utrolig stærk sammenføjning mellem metal og plastik. Dette er interessant da man traditionelt har benyttet kemisk vedhæftning (lim), evt. i kombination med simpel overfladestrukturering. I industrielle anvendelser bliver de sammenføjede komponenter ofte udsat for varierende omgivelser som f.eks. store temperatursvingninger, hvilket kan give problemer i forbindelse med kemisk vedhæftning. Afhandlingen afdækker derfor også potentielle problemer i forbindelse med de omgivelser som komponenten skal bruges i. Blandt andet studeres komponentens vandtæthed, korrosionsbestandighed og resistens overfor temperatursvingninger.

I samarbejde med Grundfos, som er verdens største pumpeproducent, er muligheden for at inkorporere en sammenføjet metal/plast komponent i deres pumpesystemer blevet undersøgt. Dette forventes at kunne øge pumpens effektivitet med op til 15%. Da næsten 20% af verdens samlede elenergi anvendes til pumpesystemer vil der kunne spares enormt meget på både elregning og $CO_2$ udslip, hvis denne teknologi bliver indlemmet i pumpeproduktionen.

# Bibliography

[1] T. Mainman, "Stimulated optical radiation in ruby", *Nature* **187**, 493 (1960).

[2] "50 years laser", http://www.50-years-laser.com.

[3] "LaserFest, celebrating 50 years of laser innovation", http://www.laserfest.org/.

[4] J. Byskov-Nielsen and P. Balling, "Laser structuring of metal surfaces: Micro-mechanical interlocking", *Applied Surface Science* **255**, 5591 (2009).

[5] "Trumpf laser Serie 3000", http://www.trumpf-laser.com/en/products/solid-state-lasers/short-pulsed-lasers/trumicro-series-3000.html.

[6] "Trumpf laser Serie 5000", http://www.trumpf-laser.com/en/products/solid-state-lasers/short-pulsed-lasers/trumicro-series-5000.html.

[7] T. Eidam, S. Hanf, E. Seise, T. V. Andersen, T. Gabler, C. Wirth, T. Schreiber, J. Limpert, and A. Tünnermann, "Femtosecond fiber CPA system emitting 830 W average output power", *Optics Letters* **35**, 94 (2010).

[8] "Grundfos press release: Grundfos is the world's largest pump manufacturer", http://www.grundfos.com/web/grfosweb.nsf/Webopslag/HMTE-5V5CZ8.

[9] "Almost 20% of the world's electricity consumption is associated with pump systems", http://www.grundfos.com/web/homecbs.nsf/Grafikopslag/pdf/$file/GF_TP_BRO_A_low.pdf.

[10] R. R. Gattass and E. Mazur, "Femtosecond laser micromachining in transparent materials", *Nature Photonics* **2**, 219 (2008).

[11] M. Neff, T. V. Kononenko, S. M. Pimenov, V. Romano, W. Luethy, and V. I. Konov, "Femtosecond laser writing of buried graphitic structures in bulk diamond", *Applied Physics A: Materials Science & Processing* **97**, 543 (2009).

[12] D. Bäuerle, *Laser Processing and Chemistry*, 3rd ed. (Springer-Verlag, Berlin, 2000).

[13] F. Dausinger, F. Lichtner, and H. Lubatschowski, *Femtosecond Technology for Technical and Medical Applications* (Springer-Verlag, Berlin, 2004).

[14] P. Balling, in *Laser Cleaning II, ed.*, edited by D. M. Kane (World Scientific Publishing Company, Singapore, 2006), p. 257.

[15] P. W. Milonni and J. H. Eberly, *Lasers* (John Wiley & Sons, New York, 1988).

[16] K. Vestentoft, J. A. Olesen, B. H. Christensen, and P. Balling, *Applied Physics A: Materials Science & Processing* **80**, 493 (2005).

[17] P. P. Pronko, S. K. Dutta, J. Squier, J. V. Rudd, D. Du, and G. Mourou, "Machining of submicron holes using a femtosecond laser at 800 nm", *Optics Communications* **114**, 106 (1995).

[18] A. Ancona, F. Roeser, K. Rademaker, J. Limpert, S. Nolte, and A. Tuennermann, "High speed laser drilling of metals using a high repetition rate, high average power ultrafast fiber CPA system", *Optics express* **16**, 8958 (2008).

[19] A. Ancona, S. Doering, C. Jauregui, F. Roeser, J. Limpert, S. Nolte, and A. Tuennermann, "Femtosecond and picosecond laser drilling of metals at high repetition rates and average powers", *Optics letters* **34**, 3304 (2009).

[20] J. Byskov-Nielsen, J.-M. Savolainen, M. S. Christensen, and P. Balling, "Ultra-short pulse laser ablation of metals: threshold fluence, incubation coefficient and ablation rates", *Applied Physics A: Materials Science & Processing* (2010).

[21] P. Balling, B. H. Christensen, J. Byskov-Nielsen, and D. Q. S. Le, "Short-pulse metal structuring: a method for modifying surface adhesion properties", *Proceedings of SPIE-Laser-based Micro- and Nanopackaging and Assembly II* **6880**, (2008).

[22] K. Vestentoft and P. Balling, "Formation of an extended nanostructured metal surface by ultrashort laser pulses: single-pulse ablation in the high-fluence limit", *Applied Physics A: Materials Science & Processing* **84**, 207 (2006).

[23] B. H. Christensen, K. Vestentoft, and P. Balling, "Short-pulse ablation rates and the two-temperature model", *Applied Surface Science* **253**, 6347 (2007).

[24] P. T. Mannion, J. Magee, E. Coyne, G. M. O'Connor, and T. J. Glynn, "The effect of damage accumulation behaviour on ablation thresholds and damage morphology in ultrafast laser micro-machining of common metals in air", *Applied Surface Science* **233**, 275 (2004).

[25] S. Nolte, C. Momma, H. Jacobs, A. Tünnermann, B. N. Chichkov, B. Wellegehausen, and H. Welling, *Journal of the Optical Society of America B* **14**, 2716 (1997).

[26] E. D. Palik, *Handbook of Optical Constants of Solids* (Academic Press, San Diego, 1985).

[27] J. M. Liu, "Simple technique for measurements of pulsed Gaussian-beam spot sizes", *Optics Letters* **7**, 196 (1982).

[28] Y. Jee, M. F. Becker, and R. M. Walser, "Laser-induced damage on single-crystal metal surfaces", *Journal of the Optical Society of America B* **5**, 648 (1988).

[29] S. Kirkwood, A. van Popta, Y. Tsui, and R. Fedosejevs, "Single and multiple shot near-infrared femtosecond laser pulse ablation thresholds of copper", *Applied Physics A: Materials Science & Processing* **81**, 729 (2005).

[30] C. S. Nielsen and P. Balling, "Deep drilling of metals with ultrashort laser pulses: A two-stage process", *Journal of Applied Physics* **99**, 093101 (2006).

[31] J. Hohlfeld, S. S. Wellershoff, J. Güdde, U. Conrad, V. Jähnke, and E. Matthias, "Electron and lattice dynamics following optical excitation of metals", *Chemical Physics* **251**, 237 (2000).

[32] A. Y. Vorobyev, V. S. Makin, and C. Guo, "Brighter Light Sources from Black Metal: Significant Increase in Emission Efficiency of Incandescent Light Sources", *Physical Review Letters* **102**, 234301 (2009).

[33] S. I. Anisimov, B. L. Kapeliovich, and T. L. Perel'man, *Soviet Physics Jetp-Ussr* **39**, 375 (1974).

[34] Z. Lin, L. V. Zhigilei, and V. Celli, "Electron-phonon coupling and electron heat capacity of metals under conditions of strong electron-phonon nonequilibrium", *Physical Review B (Condensed Matter and Materials Physics)* **77**, 075133 (2008).

[35] V. Schmidt, W. Husinsky, and G. Betz, *Applied Surface Science* **197-198**, 145 (2002).

[36] R. H. M. Groeneveld, R. Sprik, and A. Lagendijk, "Femtosecond spectroscopy of electron-electron and electron-phonon energy relaxation in Ag and Au", *Physical Review B (Condensed Matter and Materials Physics)* **51**, 11433 (1995).

[37] W. S. Fann, R. Storz, H. W. K. Tom, and J. Bokor, "Direct measurement of nonequilibrium electron-energy distributions in subpicosecond laser-heated gold films", *Physical Review Letters* **68**, 2834 (1992).

[38] D. Perez and L. J. Lewis, "Molecular-dynamics study of ablation of solids under femtosecond laser pulses", *Physical Review B (Condensed Matter and Materials Physics)* **67**, 184102 (2003).

[39] R. L. Harzic, D. Breitling, M. Weikert, S. Sommer, and C. F "Pulse width and energy influence on laser micromachining of metals in a range of 100 fs to 5 ps", *Applied Surface Science* **249**, 322 (2005).

[40] M. Hashida, A. F. Semerok, O. Gobert, G. Petite, Y. Izawa, and J. F.-. Wagner, "Ablation threshold dependence on pulse duration for copper", *Applied Surface Science* **197-198**, 862 (2002).

[41] G. A. Mourou, D. Du, S. K. Dutta, V. Elner, R. Kurtz, P. R. Lichter, and X. Liu, "Method for controlling configuration of laser induced breakdown and ablation", *US Patent* 5656186 (1997).

[42] B. N. Chichkov, C. Momma, S. Nolte, F. von Alvensleben, and A. Tünnermann, "Femtosecond, picosecond and nanosecond laser ablation of solids", *Applied Physics A: Materials Science & Processing* **63**, 109 (1996).

[43] S. S. Wellershoff, J. Hohlfeld, J. Güdde, and E. Matthias, "The role of electron-phonon coupling in femtosecond laser damage of metals", *Applied Physics A: Materials Science & Processing* **69**, S99 (1999).

[44] N. W. Ashcroft and N. D. Mermin, *Solid State Physics* (Brooks/Cole, United States of America, 1976).

[45] R. Lausten, J. A. Olesen, K. Vestentoft, and P. Balling, "Ultrafast Phenomena XIII", *Springer Series in Chemical Physics* **71**, 675 (2002).

[46] C. S. Lee, N. Koumvakalis, and M. Bass, "Spot-size dependence of laser-induced damage to diamond-turned Cu mirrors", *Applied Physics Letters* **41**, 625 (1982).

[47] J. Wang and C. Guo, "Ultrafast dynamics of femtosecond laser-induced periodic surface pattern formation on metals", *Applied Physics Letters* **87**, 251914 (2005).

[48] A. Vorobyev and C. Guo, "Enhanced absorptance of gold following multipulse femtosecond laser ablation", *Physical Review B (Condensed Matter and Materials Physics)* **72**, 195422 (2005).

[49] J. Wang and C. Guo, "Formation of extraordinarily uniform periodic structures on metals induced by femtosecond laser pulses", *Journal of Applied Physics* **100**, 023511 (2006).

[50] A. Y. Vorobyev and C. Guo, "Effects of nanostructure-covered femtosecond laser-induced periodic surface structures on optical absorptance of metals", *Applied Physics A: Materials Science & Processing* **86**, 321 (2007).

[51] A. Y. Vorobyev, V. S. Makin, and C. Guo, "Periodic ordering of random surface nanostructures induced by femtosecond laser pulses on metals", *Journal of Applied Physics* **101**, 034903 (2007).

[52] A. Y. Vorobyev and C. Guo, "Femtosecond laser structuring of titanium implants", *Applied Surface Science* **253**, 7272 (2007).

[53] C.-M. Wang, Y.-C. Chang, M.-W. Tsai, Y.-H. Ye, C.-Y. Chen, Y.-W. Jiang, Y.-T. Chang, S.-C. Lee, and D. P. Tsai, "Reflection and emission properties of an infraredemitter", *Optics Express* **15**, 14673 (2007).

[54] V. I. Emel'yanov, E. M. Zemskov, and V. N. Seminogov, "Theory of the formation of "normal" and "anomalous" gratings on the surfaces of absorbing condensed media exposed to laser radiation", *Soviet Journal of Quantum Electronics* **14**, 1515 (1984).

[55] S. A. Akhmanov, V. I. Emel'yanov, N. I. Koroteev, and V. N. Seminogov, "Interaction of powerful laser radiation with the surfaces of semiconductors and metals: nonlinear optical effects and nonlinear optical diagnostics", *Soviet Physics Uspekhi* **28**, 1084 (1985).

[56] E. Baburaj, D. Starikov, J. Evans, G. Shafeev, and A. Bensaoula, "Enhancement of adhesive joint strength by laser surface modification", *International Journal of Adhesion and Adhesives* **27**, 268 (2007).

[57] *American Institute of Physics Handbook*, 3rd ed., edited by D. E. Gray (McGraw-Hill, New York, 1972).

[58] J. Byskov-Nielsen, J. V. Boll, A. H. Holm, R. Højsholt, and P. Balling, "Ultra-high-strength micro-mechanical interlocking by injection molding into laser-structured surfaces", *International Journal of Adhesion and Adhesives* **30**, 485 (2010).

[59] A. Baldan, "Adhesively-bonded joints and repairs in metallic alloys, polymers and composite materials: Adhesives, adhesion theories and surface pretreatment", *Journal of Materials Science* **39**, 1 (2004).

[60] J. W. Murzewski, "Nonlinear Behavior of Ductile Quasi-homogeneous Solids", *International Journal of Damage Mechanics* **15**, 69 (2006).

[61] "See Data Sheet for Fortron MT9141L4", www.ticona.com.

[62] T. L. Anderson, *Fracture Mechanics: Fundamentals and Applications 3rd ed.* (CRC Press, Boca Raton, 2005).

[63] "National Institute of Standards and Technology", http://webbook.nist.gov/chemistry.

[64] J. Crank, *The Matematics of Diffusion*, 2nd ed. (Oxford University Press, Oxford, 1975).